Title

Physical Parameters of the Multiplanet Systems HD 106315 and GJ 9827* *Based on observations obtained at the W. M. Keck Observatory, which is operated jointly by the University of California and the California Institute of Technology. † †This paper i...

Journal

The Astronomical Journal, 161(1)

ISSN

0004-6256

Authors

Kosiarek, Molly R
Berardo, David A
Crossfield, Ian JM
et al.

Publication Date

2021

DOI

10.3847/1538-3881/abca39

Draft version January 6, 2021
Typeset using LaTeX **twocolumn** style in AASTeX63

Physical Parameters of the Multi-Planet Systems HD 106315 and GJ 9827*†

Molly R. Kosiarek,[1,‡] David A. Berardo,[2] Ian J. M. Crossfield,[3] Cesar Laguna,[4] Caroline Piaulet,[5] Joseph M. Akana Murphy,[1,‡] Steve B. Howell,[6] Gregory W. Henry,[7] Howard Isaacson,[8,9] Benjamin Fulton,[10] Lauren M. Weiss,[11] Erik A. Petigura,[12] Aida Behmard,[13] Lea A. Hirsch,[14] Johanna Teske,[15] Jennifer A. Burt,[16] Sean M. Mills,[17] Ashley Chontos,[18,‡] Teo Močnik,[19] Andrew W. Howard,[17] Michael Werner,[16] John H. Livingston,[20] Jessica Krick,[21] Charles Beichman,[22] Varoujan Gorjian,[16] Laura Kreidberg,[23,24] Caroline Morley,[25] Jessie L. Christiansen,[21] Farisa Y. Morales,[16] Nicholas J. Scott,[6] Jeffrey D. Crane,[26] Sharon Xuesong Wang,[27,28] Stephen A. Shectman,[26] Lee J. Rosenthal,[17] Samuel K. Grunblatt,[29,30] Ryan A. Rubenzahl,[17,‡] Paul A. Dalba,[31,§] Steven Giacalone,[32] Chiara Dane Villanueva,[4] Qingtian Liu,[4] Fei Dai,[13] Michelle L. Hill,[31] Malena Rice,[33] Stephen R. Kane,[31] Andrew W. Mayo,[32,34]

—

[1] *Department of Astronomy and Astrophysics, University of California, Santa Cruz, CA 95064, USA*
[2] *Department of Physics, and Kavli Institute for Astrophysics and Space Research, Massachusetts Institute of Technology, Cambridge, MA 02139, USA*
[3] *Department of Physics & Astronomy, University of Kansas, 1082 Malott,1251 Wescoe Hall Dr., Lawrence, KS 66045, USA*
[4] *Department of Physics, University of California, Santa Cruz, CA 95064, USA*
[5] *Department of Physics, and Institute for Research on Exoplanets, Université de Montréal, Montreal, H3T 1J4, Canada*
[6] *NASA Ames Research Center, Moffett Field, CA 94035, USA*
[7] *Center of Excellence in Information Systems, Tennessee State University, Nashville, TN 37209, USA*
[8] *501 Campbell Hall, University of California at Berkeley, Berkeley, CA 94720, USA*
[9] *Centre for Astrophysics, University of Southern Queensland, Toowoomba, QLD, Australia*
[10] *NASA Exoplanet Science Institute/Caltech-IPAC, MC 314-6, 1200 E California Blvd, Pasadena, CA 91125, USA*
[11] *Institute for Astronomy, University of Hawai'i, 2680 Woodlawn Drive, Honolulu, HI 96822, USA*
[12] *Department of Physics & Astronomy, University of California Los Angeles, Los Angeles, CA 90095, USA*
[13] *Division of Geological and Planetary Sciences, California Institute of Technology, Pasadena, CA 91125, USA*
[14] *Kavli Institute for Particle Astrophysics and Cosmology, Stanford University, Stanford, CA, USA*
[15] *Earth & Planets Laboratory, Carnegie Institution of Washington 5241 Broad Branch Road, N.W., Washington, DC 20015, USA*
[16] *Jet Propulsion Laboratory, California Institute of Technology, 4800 Oak Grove Drive, Pasadena, CA 91109, USA*
[17] *Department of Astronomy, California Institute of Technology, Pasadena, CA 91125, USA*
[18] *Institute for Astronomy, University of Hawai'i, Honolulu, HI 96822, USA*
[19] *Gemini Observatory/NSF's NOIRLab, 670 N. A'ohoku Place, Hilo, HI 96720, USA*
[20] *Department of Astronomy, University of Tokyo, 7-3-1 Hongo, Bunkyo-ku, Tokyo 113-0033, Japan*
[21] *Caltech/IPAC, 1200 E. California Blvd. Pasadena, CA 91125*
[22] *IPAC/NASA Exoplanet Science Institute, Caltech, Jet Propulsion Laboratory*
[23] *Max Planck Institute for Astronomy, Königstuhl 17, 69117 Heidelberg, Germany*
[24] *Center for Astrophysics | Harvard & Smithsonian, 60 Garden Street, Cambridge, MA, 02138, USA*
[25] *University of Texas at Austin, Austin, TX, 78712, USA*
[26] *The Observatories of the Carnegie Institution for Science 813 Santa Barbara Street, Pasadena, CA, USA 91107*
[27] *Observatories of the Carnegie Institution for Science, 813 Santa Barbara St., Pasadena, CA 91101*
[28] *Department of Astronomy, Tsinghua University, Beijing 100084, People's Republic of China*
[29] *American Museum of Natural History, 200 Central Park West, Manhattan, NY 10024, USA*
[30] *Center for Computational Astrophysics, Flatiron Institute, 162 5th Avenue, Manhattan, NY 10010, USA*
[31] *Department of Earth and Planetary Sciences, University of California, Riverside, CA 92521, USA*

Corresponding author: Molly R. Kosiarek
molly.kosiarek@gmail.com

* Based on observations obtained at the W. M. Keck Observatory, which is operated jointly by the University of California and the California Institute of Technology.

† This paper includes data gathered with the 6.5 meter Magellan Telescopes located at Las Campanas Observatory, Chile.

[32] Department of Astronomy, University of California Berkeley, Berkeley, CA 94720-3411, USA
[33] Department of Astronomy, Yale University, New Haven, CT 06511, USA
[34] Centre for Star and Planet Formation, Natural History Museum of Denmark & Niels Bohr Institute, University of Copenhagen, Øster Voldgade 5-7, DK-1350 Copenhagen K., Denmark

ABSTRACT

HD 106315 and GJ 9827 are two bright, nearby stars that host multiple super-Earths and sub-Neptunes discovered by K2 that are well suited for atmospheric characterization. We refined the planets' ephemerides through Spitzer transits, enabling accurate transit prediction required for future atmospheric characterization through transmission spectroscopy. Through a multi-year high-cadence observing campaign with Keck/HIRES and Magellan/PFS, we improved the planets' mass measurements in anticipation of Hubble Space Telescope transmission spectroscopy. For GJ 9827, we modeled activity-induced radial velocity signals with a Gaussian process informed by the Calcium II H&K lines in order to more accurately model the effect of stellar noise on our data. We measured planet masses of M_b=4.87 ± 0.37 $M_\oplus$, M_c=1.92 ± 0.49 $M_\oplus$, and M_d=3.42 ± 0.62 $M_\oplus$. For HD 106315, we found that such activity-radial velocity decorrelation was not effective due to the reduced presence of spots and speculate that this may extend to other hot stars as well ($T_{eff} > 6200$ K). We measured planet masses of M_b=10.5 ± 3.1 $M_\oplus$ and M_c=12.0 ± 3.8 $M_\oplus$. We investigated all of the planets' compositions through comparing their masses and radii to a range of interior models. GJ 9827 b and GJ 9827 c are both consistent with a 50/50 rock-iron composition, GJ 9827 d and HD 106315 b both require additional volatiles and are consistent with moderate amounts of water or hydrogen/helium, and HD 106315 c is consistent with a ∼10% hydrogen/helium envelope surrounding an Earth-like rock & iron core.

1. INTRODUCTION

Small planets cover a wide variety of compositions ranging from dense, iron-rich planets to low density planets with large hydrogen/helium envelopes. Mass and radius are degenerate with many potential compositions; measurements of atmospheric compositions can help break this degeneracy (Figueira et al. 2009; Rogers & Seager 2010).

In this paper, we characterize two planetary systems, HD 106315 and GJ 9827. These systems both consist of multiple planets transiting bright, nearby host stars. Both systems contain promising targets for atmospheric composition studies through transmission spectroscopy. Three of the planets are being observed by the Hubble Space Telescope (HST) to study their atmospheres in GO-15333 (Kreidberg et al. 2020, Benneke et al. in prep) and GO-15428 (Hedges et al. in prep). These three planets are additionally compelling targets for the James Webb Space Telescope (JWST) as determined by their transmission spectroscopy metric values (TSM, Kempton et al. 2018, HD 106315 c: 91, GJ 9827 b: 95, GJ 9827 d: 144). Precise mass measurements (20% precision) are needed to support the ongoing HST analyses and potential JWST observations as mass directly affects the observability of features and inferred properties from spectra (Batalha et al. 2019).

We measure the planet radii and update their ephemerides with Spitzer transit observations in Section 2. We describe our spectroscopy, imaging data, and update stellar parameters in Section 3. We investigate stellar activity in our radial velocity observations, K2 photometry, and ground-based photometry in Section 4. We refine the planet masses through radial velocity analyses and explore the stability of including non-zero eccentricities with N-body simulations in Section 5. Finally, we examine potential interior compositions in Section 6 by comparing the masses and radii with composition models, before concluding in Section 7.

1.1. *GJ 9827*

GJ 9827 (K2-135) is a bright (V=10.3 mag, K=7.2 mag), nearby (distance=30 pc) K6 dwarf star hosting three planets discovered in K2 Campaign 12 (Niraula et al. 2017; Rodriguez et al. 2018). Planets b and c orbit near a 3:1 resonance at 1.2 days and 3.6 days, with planet d at 6.2 days. These three planets span the gap seen in the radius distribution of small planets (Fulton et al. 2017) sized at 1.529±0.058 $R_\oplus$, 1.201±0.046 $R_\oplus$, and 1.955±0.075 $R_\oplus$ respectively. Niraula et al. (2017) additionally collected 7 radial velocity observations with the FIbrefed Echelle Spectrograph (FIES; Frandsen & Lindberg 1999; Telting et al. 2014) to vet the system and to derive stellar parameters.

The mass of planet b was first determined with radial velocity observations from the Carnegie Planet Finder Spectrograph (PFS, Crane et al. 2006, 2008, 2010)

‡ NSF Graduate Research Fellow
§ NSF Astronomy and Astrophysics Postdoctoral Fellow

on Magellan II by Teske et al. (2018) (M_b ~8 $M_\oplus$), who placed upper limits on planets c and d (M_c <2.5 $M_\oplus$, M_d <5.6 $M_\oplus$). Through additional measurements with the High Accuracy Radial velocity Planet Searcher (HARPS, Mayor et al. 2003) and the High Accuracy Radial velocity Planet Searcher for the Northern hemisphere (HARPS-N), Prieto-Arranz et al. (2018) determined the masses of all three planets (M_b=3.74±0.50 $M_\oplus$, M_c=1.47±0.59 $M_\oplus$, and M_d=2.38±0.71 $M_\oplus$). The masses of planets b and d were further refined by Rice et al. (2019) with new HARPS-N radial velocity measurements and a Gaussian process informed by the K2 light curve (M_b=4.91±0.49 $M_\oplus$ and M_d=4.04±0.84 $M_\oplus$). Both Prieto-Arranz et al. (2018) and Rice et al. (2019) discuss how the inner planets have a high density and the outer planet has a lower density, suggesting that photoevaporation or migration could have played a role in the evolution of this system; we discuss this possibility further in Section 6.

1.2. *HD 106315*

HD 106315 (K2-109) is a bright (V=8.97 mag, K=7.85 mag) F5 dwarf star hosting two planets discovered in K2 Campaign 10 (Crossfield et al. 2017; Rodriguez et al. 2017). Planet b is a small (R_b=2.40 ± 0.20 $R_\oplus$) planet with an orbital period of 9.55 days; planet c is a warm Neptune-sized (R_c=4.379 ± 0.086 $R_\oplus$) planet with an orbital period of 21.06 days.

This system was further characterized with HARPS radial velocity observations by Barros et al. (2017) to determine the planets' masses (M_b=12.6 ± 3.2 $M_\oplus$ and M_c=15.2 ± 3.7 $M_\oplus$). They concluded that HD 106315 b likely has a rocky core and decent water mass fraction whereas HD 106315 c has a substantial hydrogen-helium envelope.

Additional transits of HD 106315 c were observed with two ground based facilities: the Euler telescope (Lendl et al. 2017) and the Cerro Tololo Inter-American Observatory (CTIO, Barros et al. 2017). These measurements improved the precision on both the orbital period and the time of transit.

Later Zhou et al. (2018) investigated the system architecture through measuring the obliquity of HD 106315 c using Doppler tomography and constraining the mutual inclination of HD 106315 b through dynamical arguments. They found that these two planets both have low obliquities, consistent with the few other warm Neptunes with measured obliquities (eg. Albrecht et al. 2013).

2. SPITZER TRANSITS

Predicting precise future transit times becomes harder as more time elapses from previous transit observations and the uncertainty from the orbital period compounds. These systems contain promising targets for future atmospheric follow-up which require small uncertainties on the predicted transit time. Therefore, we collected additional transit observations on the Spitzer Space Telescope to refine the ephemerides for each planet as well as to provide a depth measurement at 4.5μm. These observations were taken as part of the K2 follow-up program 13052 (PI: Werner), using the 4.5μm channel of IRAC (Fazio et al. 2004). A single transit of each planet was observed, except for HD 106315 b which was observed twice. All of the observations were collected with 0.4 second exposures and the target placed on the 'sweet spot' of the detector.

We follow a similar analysis approach to that described in Berardo et al. (2019), which detrends the data using the Pixel Level Decorrelation method outlined in Deming et al. (2015). In brief, we first applied a median filter to each pixel in the image and calculated a background level for each frame by taking the median of the flux in an annulus centered on the point spread function. We estimated the centroid of each frame by fitting a two dimensional Gaussian to the image, and obtained a light curve using a fixed radius aperture. We varied the aperture size and performed a linear regression to determine the optimal radius; we found 2.4 pixels minimized the root mean square (RMS) of the residuals for all observations.

We modeled systematics in the light curve by weighting the nine brightest pixels individually as well as fitting for a quadratic time ramp. We then chose the combination of pixel coefficients, aperture size, and time-series binning that resulted in the smallest RMS deviation. We ran a Markov-Chain Monte Carlo (MCMC) analysis to estimate parameter uncertainties, using the systematic model in addition to a transit signal which we modeled using `batman` (Kreidberg 2015). We fixed the period of each planet to the most recent measurements (Barros et al. 2017; Rice et al. 2019) and allowed the transit depth, center, orbital inclination, and semi major axis to vary. We also left the uncertainty of the data points as a free parameter, which we found converged to the RMS scatter of the raw light curve. We held fixed the quadratic limb darkening parameters, which were determined using the tables of Claret & Bloemen (2011). The fit results are shown in Table 1 and Figure 1.

We calculated updated ephemerides (Table 2) to further refine the time of conjunction and orbital period for future atmospheric follow-up and to better constrain these values in our radial velocity fits (Section 5). We fit a straight line to the transit centers obtained from each individual observation, incorporating all ground-based

Table 1. Spitzer Transit Results

Planet	Date (UT)	Time of Conjunction (BJD)	Rp/R$_*$ (4.5μm)	Semimajor Axis (R$_*$)	Inclination (°)	Uncertainty (dex)
GJ 9827 b	2018-03-10	$2457738.82384^{+0.00081}_{-0.00080}$	$0.0225^{+0.0018}_{-0.0017}$	$7.19^{+0.56}_{-0.40}$	$87.7^{+1.8}_{-1.6}$	$-3.152^{+0.012}_{-0.012}$
GJ 9827 c	2018-03-06	$2457742.1993^{+0.0025}_{-0.0028}$	$0.0201^{+0.0023}_{-0.0020}$	$13.0^{+1.7}_{-1.3}$	$88.5^{+1.4}_{-1.1}$	$-3.307^{+0.015}_{-0.017}$
GJ 9827 d	2018-03-28	$2457740.98800^{+0.00064}_{-0.00055}$	$0.0348^{+0.0014}_{-0.0013}$	$21.8^{+2.5}_{-1.6}$	$87.72^{+0.37}_{-0.21}$	$-3.295^{+0.017}_{-0.018}$
HD 106315 b	2017-4-19	$2457586.5394^{+0.0056}_{-0.0109}$	$0.0201^{+0.0026}_{-0.0024}$	$16.4^{+5.1}_{-3.1}$	$88.4^{+2.3}_{-1.1}$	$-3.197^{+0.013}_{-0.013}$
HD 106315 b	2017-9-10	$2457586.5826^{+0.0121}_{-0.0043}$	$0.0219^{+0.0034}_{-0.0026}$	$10.4^{+2.2}_{-1.3}$	$87.6^{+3.0}_{-1.7}$	$-3.155^{+0.010}_{-0.010}$
HD 106315 c	2017-4-20	$2457569.0103^{+0.0012}_{-0.0012}$	$0.0329^{+0.0013}_{-0.0012}$	$29.5^{+5.7}_{-4.2}$	$88.89^{+0.69}_{-0.51}$	$-3.189^{+0.012}_{-0.012}$

Table 2. Ephemerides Update

Planet	Time of Conjunction (BJD)	Period (days)
GJ 9827 b	2457738.82586±0.00026	1.2089765±2.3e-06
GJ 9827 c	2457742.19931±0.00071	3.648096±2.4e-05
GJ 9827 d	2457740.96114±0.00044	6.20183±1.0e-05
HD 106315 b	2457586.5476±0.0025	9.55287±0.00021
HD 106315 c	2457569.01767±0.00097	21.05652±0.00012

published transits thus far (Lendl et al. 2017; Barros et al. 2017). These planets will be accessible for future transmission spectroscopy observations throughout the JWST era. As an example, the transit time uncertainty in 2025 is under two hours for all five planets (GJ 9827 b: 0.1hr, GJ 9827 c: 0.5hr, GJ 9827 d: 0.1hr, HD 106315 b: 1.7hr, HD 106315 c: 0.4hr).

3. STELLAR PARAMETERS AND COMPANION REFINEMENT

3.1. *Spectroscopy*

We collected radial velocity measurements of GJ 9827 and HD 106315 with the High Resolution Echelle Spectrometer (HIRES, Vogt et al. 1994) on the Keck I Telescope on Maunakea. These exposures were taken through an iodine cell for wavelength calibration (Butler et al. 1996). The HIRES data collection, reduction, and analysis followed the California Planet Search method described in Howard et al. (2010).

We obtained 92 measurements of GJ 9827 with HIRES between 2017 September 22 and 2020 January 8 (Table 7). These data were collected with the C2 decker (14″x0.861″, resolution=50k) with a typical signal-to-noise radio (SNR) of 200/pixel (250k on the exposure meter, median exposure time of 18.5 minutes). We also collected a higher resolution template observation with the B3 decker (14″x0.574″, resolution=67k) on 2017 December 30 with a SNR of 200/pixel without the iodine cell. Both the C2 and B3 decker allow for sky subtraction which is important for the quality of the radial velocities for a V=10 mag star. We included an additional 142 measurements in our GJ 9827 analysis, for a total of 234 measurements: 7 from FIES (Niraula et al. 2017), 36 from PFS (Teske et al. 2018), 35 from HARPS (Prieto-Arranz et al. 2018), and 64 from HARPS-N (Prieto-Arranz et al. 2018; Rice et al. 2019).

We obtained 352 measurements of HD 106315 with HIRES between 2016 December 23 and 2020 Febuary 1 (Table 8); 53 of these observations were previously published in Crossfield et al. (2017). These data were collected with the B5 decker (3.5″x0.861″, resolution=50k) with a typical SNR of 200/pixel (250k on the exposure meter, median exposure time of 4.8 minutes). Data were typically taken in groups of three consecutive observations to mitigate p-mode oscillations; Barros et al. (2017) estimated p-mode periods of ∼20 minutes whereas Chaplin et al. (2019) estimates timescales to be ∼30 minutes. When possible, multiple visits separated by an hour were taken to improve precision due to the high $v \sin i$; these data were then binned in nightly bins to average over short-timescale activity. We also collected a higher resolution template observation with the B3 decker on 2016 December 24. The template was a triple exposure with a total SNR of 346/pixel (250k each on the exposure meter) without the iodine cell.

We obtained 25 measurements of HD 106315 with PFS between 2017 January 6 and 2018 June 30 (Table 8). Data taken prior to 2018 February were taken with the 0.5″slit (resolution∼80k); a single observation with an exposure time of 10 to 25 minutes was taken per night. After a PFS upgrade in 2018 February, multiple exposures were taken with the 0.3″slit (resolution∼130k). As with the HIRES data, we binned these consecutive observations for our analysis. An iodine-free template, consisting of three 1000s exposures, was taken with the 0.3″slit on 2018 June 27. The PFS data were reduced using a custom IDL pipeline and velocities extracted based on the methodology described in Butler et al. (1996).

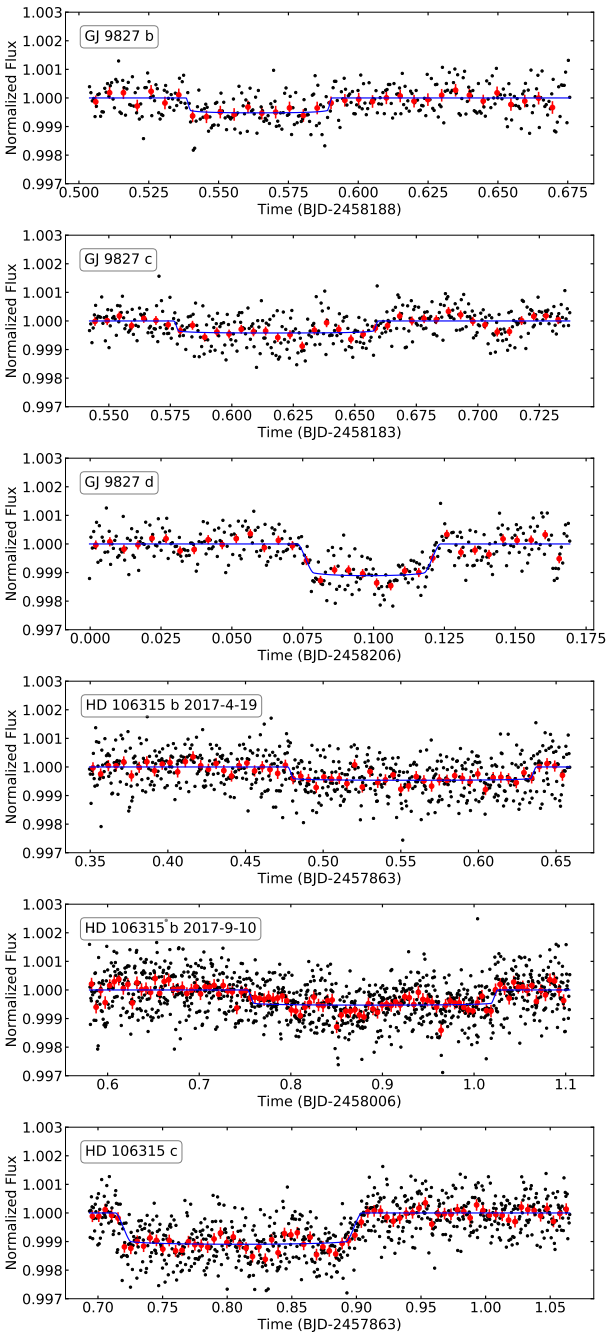

Figure 1. Spitzer transits for GJ 9827 b, c, d and HD 106315 b, c. Data (black points), binned data (red circles), and model fit (blue line) are shown.

We additionally include 84 measurements from HARPS (Barros et al. 2017), for a total of 461 measurements (160 binned points) in our HD 106315 analysis. We collected 125 measurements on the Automated Planet Finder (APF, Radovan et al. 2014; Vogt et al. 2014) but do not include them in the analysis due to the high scatter (30 m/s nightly RMS, 7.3 m/s RV uncertainty), listed in Table 8.

We updated the stellar parameters for GJ 9827 and HD 106315 to incorporate the latest measurements, especially the Gaia DR2 parallaxes (Gaia Collaboration et al. 2016, 2018; Luri et al. 2018). We used multiband stellar photometry (Gaia G and 2MASS JHK), the Gaia parallax, and a stellar effective temperature and metallicity derived from Keck/HIRES spectra via the SpecMatch-Emp tool (Yee et al. 2017). The SpecMatch-Emp values are $T_{\rm eff}$ = 6318±110 K and 4195±70 K, and [Fe/H]= -0.21 ± 0.09 and -0.29 ± 0.09 for HD 106315 and GJ 9827, respectively. We input the above values into the isoclassify tool using the grid-mode option (Huber et al. 2017) to derive the stellar parameters listed in Table 3.

Table 3. Stellar Parameters

Parameter	units	GJ 9827	HD 106315
[Fe/H]	dex	-0.26±0.08	-0.22±0.09
M_*	$M_{\rm Sun}$	0.593±0.018	1.154±0.042
R_*	$R_{\rm Sun}$	0.579±0.018	1.269±0.024
log g	dex	4.682±0.021	4.291±0.025
$T_{\rm eff}$	K	4294±52	6364±87

3.2. *HD 106315 Imaging*

The discovery papers for HD 106315 included seeing limited imaging data and K-band Keck/NIRC2 infrared adaptive optics imaging to rule out nearby stellar companions (Rodriguez et al. 2017; Crossfield et al. 2017). We include here additional high contrast imaging data to improve the magnitude contrast constraints on nearby companions.

We observed HD 106315 on 2019 June 20 UT using the Zorro speckle interferometric instrument[1] mounted on the 8-meter Gemini South telescope located on the summit of Cerro Pachon in Chile. Zorro simultaneously observes in two bands, one centered at 832nm with a width of 40nm and the other centered at 562nm with a width of 54nm, obtaining diffraction limited images with inner working angles 0.017 and 0.026 arcseconds, respectively. Our data set consisted of 3 minutes of total integration time taken as sets of 1000 × 0.06 sec images. All the images were combined and subjected to Fourier analysis leading to the production of final data

[1] https://www.gemini.edu/sciops/instruments/alopeke-zorro/

products including speckle reconstructed imagery (see Howell et al. 2011). Figure 2 shows the 5-sigma contrast curves in both filters for the Zorro observation and includes an inset showing the 832 nm reconstructed image. The speckle imaging results confirm HD 106315 to be a single star to contrast limits of 5–8.6 magnitudes, ruling out main sequence companions fainter than HD 106315 itself within the spatial limits of 2 to 125 AU.

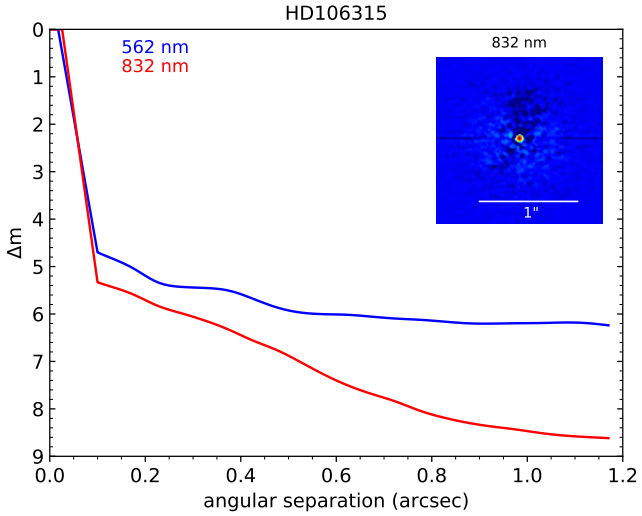

Figure 2. Gemini-S/Zorro speckle-imaging contrast curve for HD 106315 in 832nm (red) and 562nm (blue) including an inset image of the 832nm observation. No stellar companions or background sources are seen in these data.

4. STELLAR ACTIVITY ANALYSIS

Variability in the brightness and velocity fields across the stellar disk results in line shape variations and apparent radial velocity shifts. Stellar activity with timescales comparable to planet orbital periods is a particular problem for radial velocity analyses as these signals can appear as additional Keplerian signals or can affect the fit amplitudes of the planet signals (eg. Fulton et al. 2015). For our two systems, we focus on the component of stellar activity related to stellar rotation, as these signals have similar timescales to the transiting planet signals.

Stellar activity can be tracked in radial velocity data using certain stellar lines as activity indicators. The Calcium II H&K lines are often used for this purpose (S_{HK}, Isaacson & Fischer 2010), whereas H-alpha may be more successful for cooler stars (Robertson et al. 2013). Another method is to use photometry to characterize the stellar activity and then subsequently fold the activity information into radial velocity fits (Haywood et al. 2014). For the Sun, there is a connection between stellar activity information derived from photometry, activity indicators, and radial velocity data (Kosiarek & Crossfield 2020). Here we investigate how stellar activity manifests in the K2 light curve, the Calcium II H&K and H-alpha stellar lines, and our radial velocity data.

4.1. *GJ 9827 Stellar Activity*

The K2 light curve for GJ 9827 shows quasi periodic variation with signs of active region evolution between rotation cycles (Figure 3). The K2 photometry shown in this paper was produced using k2phot (Petigura et al. 2015, 2017). A Lomb-Scargle periodogram of the K2 data shows two strong peaks around 15 and 30 days consistent with previous works, one peak is likely the rotation period and the other a harmonic. We consider both peaks since stellar rotation periods often do not appear as the highest peak in a periodogram (Nava et al. 2019). The shorter period is favored by Niraula et al. (2017) from the $v \sin i$ measurement, whereas the longer period is favored by Rodriguez et al. (2018); Teske et al. (2018); Prieto-Arranz et al. (2018); Rice et al. (2019) from a combination of periodogram, autocorrelation, and Gaussian process analyses on the light curve as well as from the inferred age of GJ 9827.

The Keck/HIRES S_{HK} and radial velocity data shown in Figure 3, both reveal a tenuous stellar rotation signal at 30 days, consistent with the longer peak in the K2 light curve peridogram. In agreement with previous findings, we conclude that this 30 day signal is likely caused by stellar rotation, as it is present in both the S_{HK} data and the photometry. Since there is power at the same period in our radial velocity data, we need to account for this signal in our radial velocity analysis in order to derive accurate mass measurements for the planets. We mitigated this signal using a Gaussian process, as described below in Section 5.1.

4.2. *HD 106315 Stellar Activity*

Similar to GJ 9827, we aim to understand the stellar activity component of the radial velocity data through investigating the possible relationships between the K2 light curve, the Calcium II H&K and H-alpha stellar lines, and our radial velocity data. The projected rotational velocity measurement ($v \sin i = 13.2 \pm 1$ km s^{-1}) combined with the obliquity measurement ($\lambda = -10.9 \pm 3.7$, Zhou et al. 2018) suggests a stellar rotation period of 4.78±0.15 days.

HD 106315 was observed in K2 Campaign 10; this campaign had a 14 day data gap resulting in 49 days of contiguous data. With a 4.8 day rotation period, the shorter campaign should not impact our conclusions about stellar activity from this photometry. The K2

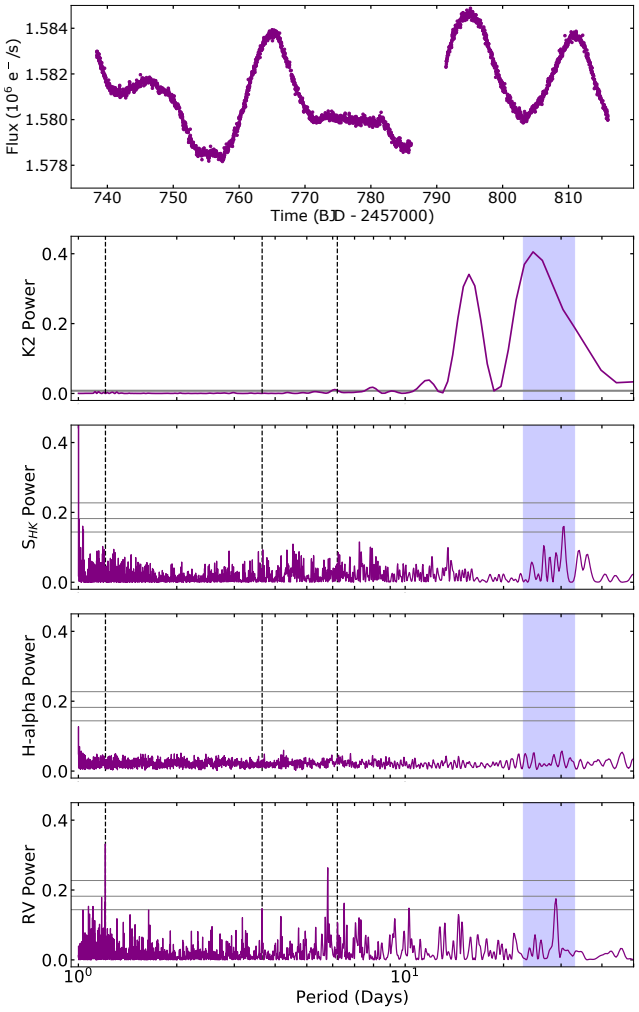

Figure 3. Activity analysis for GJ 9827 from K2 photometry and HIRES spectroscopy. There are clear stellar rotation and active region evolution signals visible by eye in the K2 photometry. The Lomb-Scargle periodograms of the K2 photometry, S_{HK}, H-alpha, and radial velocity data include false alarm probabilities of 0.5, 0.1, 0.01 (horizontal lines), stellar rotation (blue shaded area), and planet orbital periods (dashed lines). There is a stellar rotation signal at 30 days in the S_{HK} and radial velocity data, consistent with the broad peak in the K2 photometry.

light curve (Figure 4) has low photometric variability; the periodogram shows a small peak near the stellar rotation period at 4.8 days and a larger peak at the second harmonic of the rotation period at 9.6 days.

We next investigated the potential radial velocity signal from the stellar rotation by examining the S_{HK} and H-alpha data in the HIRES spectra (Table 8). We find no significant peaks near 4.8 days or elsewhere in Lomb-Scargle periodograms of the HIRES activity indicators and radial velocity data (Figure 4). The absence of these signals suggests that the stellar rotation is not contributing a significant stellar activity signal to the radial velocity measurements, potentially attributed to the low spot coverage of this F star ($< 1\%$, Kreidberg et al. 2020).

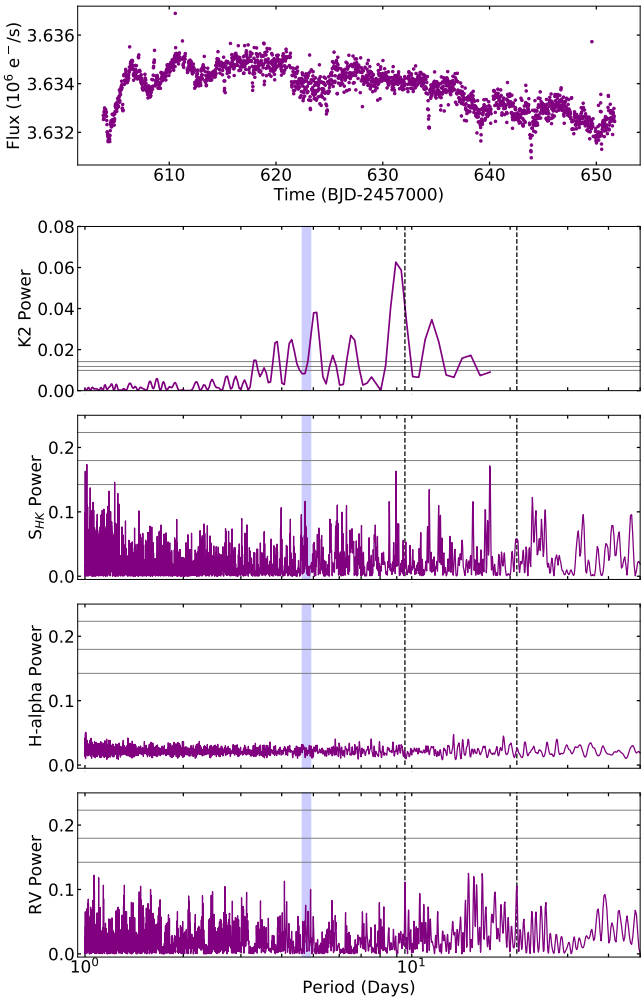

Figure 4. Activity analysis for HD 106315 from K2 photometry and HIRES spectroscopy. The Lomb-Scargle periodograms of the photometry, S_{HK}, H-alpha, and radial velocity data include false alarm probabilities of 0.5, 0.1, 0.01 (horizontal lines), stellar rotation period (thick blue line), and planet orbital periods (dashed lines). There are peaks near the rotation period and second harmonic in the K2 photometry, we find no similar peaks in the HIRES activity indicators or radial velocity data.

4.3. *Ground-based Photometry*

Stellar photometry of both systems was collected from the Fairborn Observatory in Arizona to lengthen the photometry baseline from which to look for stellar variability.

Photometry of GJ 9827 was collected with the Tennessee State University Celestron C14 0.36 m Automated Imaging Telescope (AIT, Henry 1999; Eaton et al. 2003). A total of 74 observations were collected from 2018 September 22 to 2020 January 27th with the Cousins R filter (Table 9). The differential magnitudes were computed by subtracting the average brightness of 7 comparison stars in the same field of view. A frequency spectrum of the observations show no significant periodicities between 1 and 100 days; the observations scatter about their mean with a standard deviation of 0.00372 mag.

Photometry of HD 106315 was collected with the T12 0.80 m Automatic Photoelectric Telescope (APT); the T12 APT is essentially identical in construction and operation to the T8 0.8 m APT described in Henry (1999). A total of 43 observations of HD 106315 were collected between 2018 February 9 and 2018 June 7 in both the Stromgren b and y filters by T12's two-channel photometer (Table 10). The two filters were averaged together into the (b+y)/2 "filter" to increase the data precision. The differential magnitudes were calculated using three comparison stars: HD 105374, HD 105589, and HD 106965. A frequency spectrum of the observations show no significant periodicities between 1 and 100 days; the observations scatter about their mean with a standard deviation of 0.00256 mag.

5. RADIAL VELOCITY ANALYSIS

We analyzed the radial velocity data for these two systems with `radvel`[2] (Fulton et al. 2018). `radvel` models Keplerian orbits and optional Gaussian processes to fit radial velocity data. The fit is performed through a maximum-likelihood function and errors are determined with an MCMC analysis. We use the default number of walkers, number of steps, and criteria for burn-in and convergence as described in Fulton et al. (2018).

For both systems, we first model the radial velocity data including circular Keplerian orbits for all of the transiting planets; we include a Gaussian prior on the orbital period (P) and time of transit ($T_{\rm conj}$) from our updated ephemerides in Section 2. The semi-amplitudes (K) reported from these analyses refer to the motion of the star induced by the orbiting planet. Afterwards, we test models including a trend ($\dot{\gamma}$), curvature ($\ddot{\gamma}$), and planet eccentricities (e, ω). We used the Akaike information criterion corrected for small samples sizes (AIC) to evaluate if the fit improved sufficiently to justify the additional free parameters; a lower AIC indicates an improved fit.

[2] https://radvel.readthedocs.io/

5.1. *Radial Velocity Analysis for GJ 9827*

There is evidence of stellar activity in our radial velocity data from the periodogram analysis in Section 4. We include a Gaussian process with a quasi-periodic kernel to model this activity signal in our radial velocity fit. The kernel has the form

$$k(t,t') = \eta_1^2 \exp\left[-\frac{(\mathrm{t}-\mathrm{t}')^2}{\eta_2^2} - \frac{\sin^2(\frac{\pi(\mathrm{t}-\mathrm{t}')}{\eta_3})}{2\eta_4^2}\right], \quad (1)$$

where the hyperparameter η_1 is the amplitude of the covariance function, η_2 is the active region evolutionary time scale, η_3 is the period of the correlated signal, and η_4 is the length scale of the periodic component. We explore these hyperparameters for this system by performing a maximum likelihood fit to the K2 light curve, $\mathrm{S_{HK}}$, and H-alpha data with the quasi-periodic kernel (Equation 1), then determine the errors through an MCMC analysis.

The K2 light curve fit is well constrained by the Gaussian process and produces a stellar rotation period consistent with the periodogram analysis of this data (η_3=$28.62^{+0.48}_{-0.38}$). The H-alpha data has very low variation; it is not well fit by this kernel and does not produce meaningful posteriors.

The $\mathrm{S_{HK}}$ data is well fit by this quasi-periodic kernel and produces a stellar rotation period (η_3) consistent with our periodogram analysis in Section 4. The photometry and the $\mathrm{S_{HK}}$ data both produce consistent posteriors; we choose to adopt the posteriors from the $\mathrm{S_{HK}}$ fit because these data are taken simultaneously with the radial velocity data and are therefore a direct indicator of the chromospheric magnetic activity. The posteriors on the parameters from our $\mathrm{S_{HK}}$ fit are: $\gamma_{S_{\rm HK}} = 0.646^{+0.027}_{-0.026}$, $\sigma_{S_{\rm HK}} = 0.0183^{+0.0035}_{-0.0032}$, $\eta_1 = 0.079^{+0.017}_{-0.012}$, $\eta_2 = 94^{+50}_{-25}$ days, $\eta_3 = 29.86^{+0.78}_{-0.83}$ days, and $\eta_4 = 0.587^{+0.14}_{-0.096}$.

We then performed a Gaussian process fit on the radial velocity data including priors on η_2, η_3, and η_4 equivalent to the $S_{\rm HK}$ fit posteriors. We tested fits including a trend, curvature, and planet eccentricities but reject all of these models due to their higher AIC values. These tested fits resulted in semi-amplitudes for all three planets consistent to 1σ for planets b and d, and 2σ for planet c with the circular 3-planet Gaussian process fit.

We present our GJ 9827 results in Table 4. We list the results from a circular 3-planet case with and without a Gaussian process for comparison, and adopt the fit including the Gaussian process shown in Figure 5. We measure masses for these planets to be M_b=4.87 ± 0.37 $M_\oplus$, M_c=1.92 ± 0.49 $M_\oplus$, and M_d=3.42 ± 0.62 $M_\oplus$.

5.2. *Radial Velocity Analysis for HD 106315*

For HD 106315, the circular 2-planet fit is favored by the AIC over fits with a trend, curvature, or planet eccentricities; results are listed in Table 5 and the fit is displayed in Figure 6. In agreement with Barros et al. (2017), we do not see evidence of the trend suggested in Crossfield et al. (2017) with an AIC value 1.25 larger than the circular case. We determine masses for the HD 106315 system to be M_b=10.5 ± 3.1 $M_\oplus$ and M_c=12.0 ± 3.8 $M_\oplus$.

In contrast with our GJ 9827 analysis, we choose not to include a Gaussian process in our HD 106315 fit as we do not see evidence for stellar rotation induced activity contamination in the activity indicators or radial velocity data. We suspect the low spot coverage of HD 106315 (< 1%, Kreidberg et al. 2020) is why we see a small rotation signal in the photometry and a lack of this signal in our radial velocity data. Barros et al. (2017) does use a Gaussian process for their analysis of HD 106315. The derived Gaussian process period is 2.8 days and their full width half maximum (FWHM) measurements also show a similar periodicity leading them to believe that this signal arises from stellar activity. At the time, Zhou et al. (2018) had not yet measured the obliquity; therefore, Barros et al. (2017) hypothesized that this 2.8 day signal was the stellar rotation period or half of the rotation period.

If this signal is associated with stellar activity, it is possible that their high cadence radial velocity run is more sensitive to this activity than our data collection spanning multiple years. The HARPS measurements were collected on 47 nights over three months, whereas we have 94 nights of HIRES measurements over three years. It is also possible that the Gaussian process used by Barros et al. (2017) had fit spurious noise instead of a stellar activity signal; the 2.8 day signal is too short to be the rotation period or half of the rotation period. Hotter stars (T_{eff} >6200 K) often have shallow convective envelopes and inefficient magnetic dynamos which result in fewer spots on the stellar surface (Kraft 1967). Therefore, hotter stars like HD 106315 may not have enough starspots for this type of Gaussian process to be effective.

For completeness, we perform a Gaussian process fit on the HD 106315 radial velocity data. We first fit the

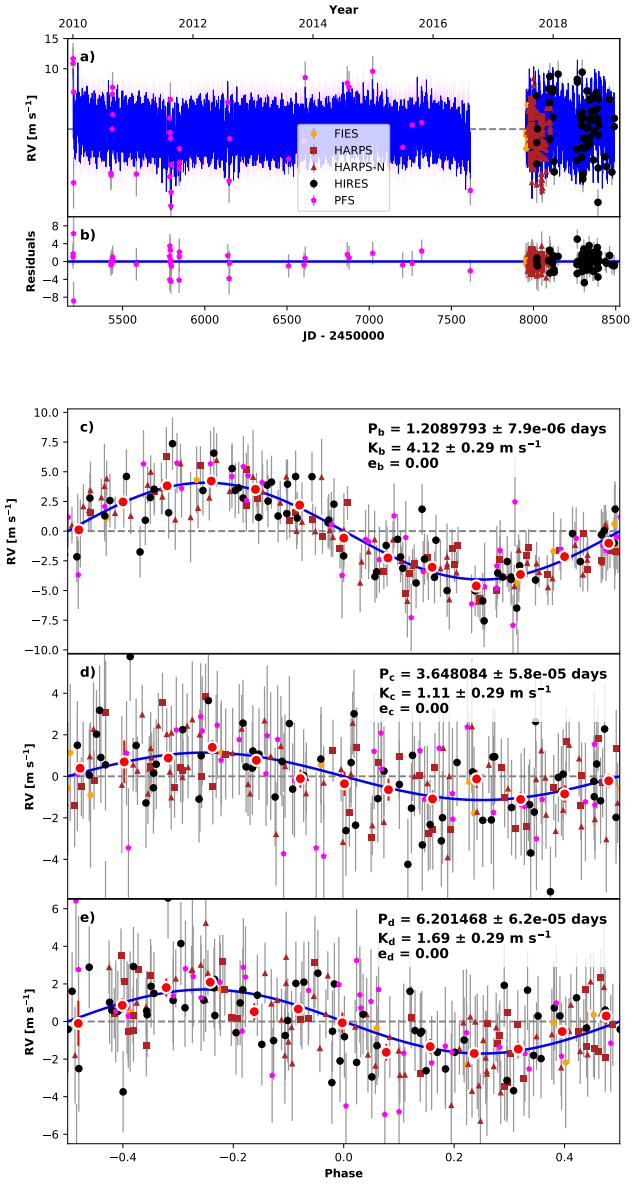

Figure 5. Best-fit 3-planet Keplerian orbital model with a Gaussian process for GJ 9827. The thin blue line is the best-fit one-planet model with the mean Gaussian process model; the colored area surrounding this line includes the 1σ maximum-likelihood Gaussian process uncertainties. We add in quadrature the RV jitter terms listed in Table 4 with the measurement uncertainties for all RVs. **b)** Residuals to the best fit 2-planet model. **c)** RVs phase-folded to the ephemeris of planet b; the Keplerian orbit models for the other planets have been subtracted. Red circles are the same velocities binned in 0.08 units of orbital phase. **d)** RVs phase-folded to the ephemeris of planet c. **e)** RVs phase-folded to the ephemeris of planet d.

Table 4. GJ 9827 Radial Velocity Fit Parameters

Parameter	Name (Units)	Keplerian fit	Gaussian Process fit (adopted)
Orbital Parameters			
P_b	Period (days)	$1.2089765^{+2.2e-06}_{-2.3e-06}$	$1.2089765 \pm 2.3e-06$
$T\mathrm{conj_b}$	Time of Conjunction (BJD)	$2457738.82586 \pm 0.00026$	$2457738.82586 \pm 0.00026$
R_b	Radius ($\mathrm{R}_\oplus$)	$\equiv$1.529±0.058	$\equiv$1.529±0.058
e_b	Eccentricity	$\equiv 0.0$	$\equiv 0.0$
ω_b	Argument of Periapse	$\equiv 0.0$	$\equiv 0.0$
K_b	Semi-Amplitude (m s^{-1})	3.5 ± 0.32	4.1 ± 0.3
a_b	Semimajor Axis (AU)	0.01866 ± 0.00019	0.01866 ± 0.00019
M_b	Mass ($\mathrm{M}_\oplus$)	$4.12^{+0.39}_{-0.38}$	4.87 ± 0.37
ρ_b	Density (g cm^{-3})	$6.32^{+1.0}_{-0.87}$	$7.47^{+1.1}_{-0.95}$
P_c	Period (days)	$3.648095^{+2.5e-05}_{-2.4e-05}$	$3.648095 \pm 2.4e-05$
$T\mathrm{conj_c}$	Time of Conjunction (BJD)	$2457742.19927 \pm 0.00071$	$2457742.19929^{+0.00072}_{-0.00071}$
R_c	Radius ($\mathrm{R}_\oplus$)	$\equiv$1.201±0.046	$\equiv$1.201±0.046
e_c	Eccentricity	$\equiv 0.0$	$\equiv 0.0$
ω_c	Argument of Periapse	$\equiv 0.0$	$\equiv 0.0$
K_c	Semi-Amplitude (m s^{-1})	1.28 ± 0.32	1.13 ± 0.29
a_c	Semimajor Axis (AU)	$0.03896^{+0.00039}_{-0.0004}$	$0.03896^{+0.00039}_{-0.0004}$
M_c	Mass ($\mathrm{M}_\oplus$)	$2.17^{+0.54}_{-0.55}$	1.92 ± 0.49
ρ_c	Density (g cm^{-3})	$6.9^{+2.0}_{-1.8}$	$6.1^{+1.8}_{-1.6}$
P_d	Period (days)	$6.20183 \pm 1e-05$	$6.20183 \pm 1e-05$
$T\mathrm{conj_d}$	Time of Conjunction (BJD)	$2457740.96114 \pm 0.00044$	$2457740.96114^{+0.00045}_{-0.00044}$
R_d	Radius ($\mathrm{R}_\oplus$)	$\equiv$1.955±0.075	$\equiv$1.955±0.075
e_d	Eccentricity	$\equiv 0.0$	$\equiv 0.0$
ω_d	Argument of Periapse	$\equiv 0.0$	$\equiv 0.0$
K_d	Semi-Amplitude (m s^{-1})	1.63 ± 0.31	1.7 ± 0.3
a_d	Semimajor Axis (AU)	$0.0555^{+0.00056}_{-0.00057}$	$0.0555^{+0.00055}_{-0.00057}$
M_d	Mass ($\mathrm{M}_\oplus$)	3.29 ± 0.64	3.42 ± 0.62
ρ_d	Density (g cm^{-3})	$2.41^{+0.58}_{-0.52}$	$2.51^{+0.57}_{-0.51}$
Instrument Parameters			
γ_{HIRES}	Mean center-of-mass (m s−1)	$-1.87^{+0.38}_{-0.39}$	$-2.4^{+1.3}_{-1.4}$
γ_{HARPS}	Mean center-of-mass (m s−1)	31946.64 ± 0.37	$31947.7^{+4.0}_{-3.6}$
$\gamma_{\mathrm{HARPS-N}}$	Mean center-of-mass (m s−1)	$31948.64^{+0.43}_{-0.42}$	$31950.2^{+2.7}_{-2.6}$
γ_{PFS}	Mean center-of-mass (m s−1)	0.28 ± 0.86	0.6 ± 1.2
γ_{FIES}	Mean center-of-mass (m s−1)	$31775.5^{+1.1}_{-1.2}$	31775.6 ± 1.5
σ_{HIRES}	Jitter (m s^{-1})	$3.45^{+0.32}_{-0.27}$	$2.15^{+0.49}_{-0.43}$
σ_{HARPS}	Jitter (m s^{-1})	$1.65^{+0.39}_{-0.35}$	$0.91^{+0.44}_{-0.45}$
$\sigma_{\mathrm{HARPS-N}}$	Jitter (m s^{-1})	$2.79^{+0.39}_{-0.35}$	$0.74^{+0.44}_{-0.45}$
σ_{PFS}	Jitter (m s^{-1})	$4.68^{+0.75}_{-0.62}$	4.0 ± 1.1
σ_{FIES}	Jitter (m s^{-1})	$0.0001^{+0.0016}_{-0.0001}$	$0.035^{+2.6}_{-0.035}$
GP Parameters			
$\eta_{1,\mathrm{HIRES}}$	GP Amplitude (m s^{-1})	N/A	$3.7^{+1.2}_{-1.0}$
$\eta_{1,\mathrm{HARPS}}$	GP Amplitude (m s^{-1})	N/A	$5.3^{+3.5}_{-2.2}$
$\eta_{1,\mathrm{HARPS-N}}$	GP Amplitude (m s^{-1})	N/A	$5.1^{+2.3}_{-1.5}$
$\eta_{1,\mathrm{PFS}}$	GP Amplitude (m s^{-1})	N/A	4.0 ± 1.1
$\eta_{1,\mathrm{FIES}}$	GP Amplitude (m s^{-1})	N/A	$0.035^{+2.6}_{-0.035}$
η_2	Evolutionary Timescale (days)	N/A	82^{+17}_{-14}
η_3	Period of the Correlated Signal (days)	N/A	$28.62^{+0.48}_{-0.38}$
η_4	Lengthscale	N/A	$0.418^{+0.082}_{-0.065}$

Derived parameters use M_*=0.593 ± 0.018, R_*=0.579 ± 0.019 (This work), $\mathrm{R}_b/\mathrm{R}_*$=0.02420 ± 0.00044, $\mathrm{R}_c/\mathrm{R}_*$=0.01899 ± 0.00036, $\mathrm{R}_d/\mathrm{R}_*$=0.03093 ± 0.00062 (Rodriguez et al. 2018).

Table 5. HD 106315 Radial Velocity Fit Parameters

Parameter	Name (Units)	Keplerian fit (adopted)	Gaussian Process fit
Orbital Parameters			
P_b	Period (days)	9.55288 ± 0.00021	$9.55288^{+0.00019}_{-0.00021}$
$T\mathrm{conj_b}$	Time of Conjunction (BJD)	$2457586.5476^{+0.0024}_{-0.0025}$	$2457586.5479^{+0.003}_{-0.0026}$
R_b	Radius ($\mathrm{R}_\oplus$)	$\equiv 2.40 \pm 0.20$	$\equiv 2.40 \pm 0.20$
e_b	Eccentricity	$\equiv 0.0$	$\equiv 0.0$
ω_b	Argument of Periapse	$\equiv 0.0$	$\equiv 0.0$
K_b	Semi-Amplitude (m s^{-1})	$2.88^{+0.85}_{-0.84}$	$2.91^{+0.79}_{-0.85}$
a_b	Semimajor Axis (AU)	$0.0924^{+0.0011}_{-0.0012}$	$0.0924^{+0.0011}_{-0.0012}$
M_b	Mass ($\mathrm{M}_\oplus$)	10.5 ± 3.1	$10.6^{+2.9}_{-3.1}$
ρ_b	Density (g cm^{-3})	$4.1^{+1.9}_{-1.4}$	$4.1^{+1.8}_{-1.4}$
P_c	Period (days)	21.05652 ± 0.00012	21.05653 ± 0.00012
$T\mathrm{conj_c}$	Time of Conjunction (BJD)	$2457569.01767^{+0.00097}_{-0.00096}$	$2457569.0178^{+0.0012}_{-0.001}$
R_c	Radius ($\mathrm{R}_\oplus$)	$\equiv 4.379 \pm 0.086$	$\equiv 4.379 \pm 0.086$
e_c	Eccentricity	$\equiv 0.0$	$\equiv 0.0$
ω_c	Argument of Periapse	$\equiv 0.0$	$\equiv 0.0$
K_c	Semi-Amplitude (m s^{-1})	2.53 ± 0.79	$2.61^{+0.74}_{-0.87}$
a_c	Semimajor Axis (AU)	$0.1565^{+0.0019}_{-0.002}$	$0.1565^{+0.0019}_{-0.002}$
M_c	Mass ($\mathrm{M}_\oplus$)	12.0 ± 3.8	$12.4^{+3.5}_{-4.2}$
ρ_c	Density (g cm^{-3})	$0.78^{+0.26}_{-0.25}$	$0.81^{+0.24}_{-0.27}$
Instrument Parameters			
γ_{HIRES}	Mean center-of-mass (m s−1)	$-2.48^{+0.96}_{-0.97}$	$-2.7^{+1.0}_{-1.1}$
γ_{HARPS}	Mean center-of-mass (m s−1)	$-3462.94^{+0.7}_{-0.71}$	$-3462.77^{+1.1}_{-0.87}$
γ_{PFS}	Mean center-of-mass (m s−1)	$-2.9^{+2.8}_{-2.7}$	$-2.5^{+3.2}_{-3.3}$
σ_{HIRES}	Jitter (m s^{-1})	$8.33^{+0.85}_{-0.79}$	$6.4^{+1.2}_{-1.1}$
σ_{HARPS}	Jitter (m s^{-1})	$2.94^{+0.94}_{-1.0}$	$2.3^{+1.0}_{-1.4}$
σ_{PFS}	Jitter (m s^{-1})	$9.4^{+2.6}_{-2.3}$	$4.0^{+4.6}_{-2.7}$
GP Parameters			
$\eta_{1,\mathrm{HIRES}}$	GP Amplitude (m s^{-1})	N/A	$5.2^{+1.1}_{-1.7}$
$\eta_{1,\mathrm{HARPS}}$	GP Amplitude (m s^{-1})	N/A	$2.3^{+1.0}_{-1.4}$
$\eta_{1,\mathrm{PFS}}$	GP Amplitude (m s^{-1})	N/A	$4.0^{+4.6}_{-2.7}$
η_2	Evolutionary Timescale (days)	N/A	$5.27^{+0.54}_{-0.65}$
η_3	Period of the Correlated Signal (days)	N/A	$4.5^{+0.49}_{-0.65}$
η_4	Lengthscale	N/A	$0.56^{+0.036}_{-0.04}$

Derived parameters use M_*=1.154 ± 0.043, R_*=1.269 ± 0.024 (This work), $\mathrm{R}_b/\mathrm{R}_*$=0.01708 ± 0.00135 (Crossfield et al. 2017), $\mathrm{R}_c/\mathrm{R}_*$=0.031636 ± 0.0001834 (Kreidberg et al. 2020).

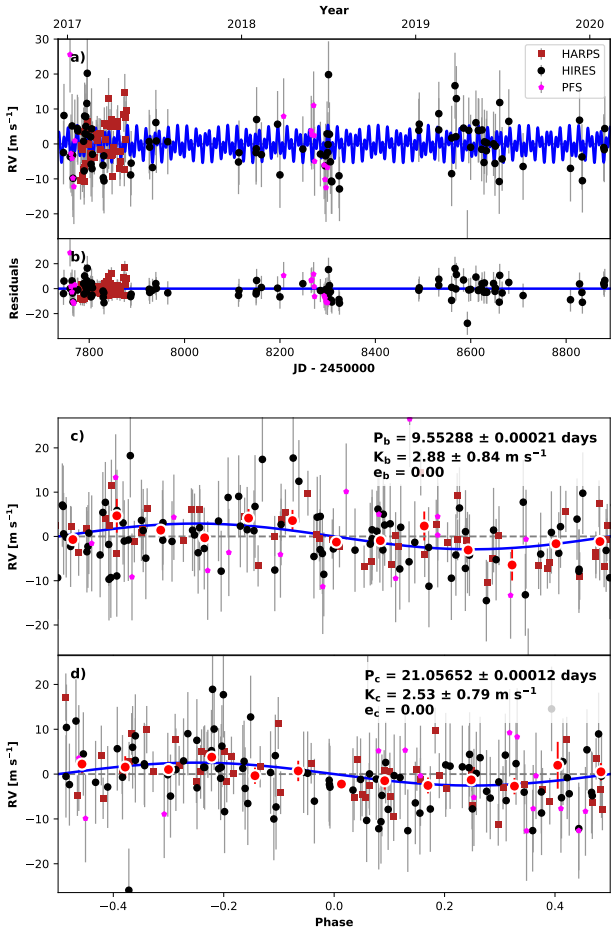

Figure 6. Best-fit 2-planet Keplerian orbital model for HD 106315. The thin blue line is the best fit 2-planet model. We add in quadrature the RV jitter terms listed in Table 5 with the measurement uncertainties for all RVs. **b)** Residuals to the best fit 2-planet model. **c)** RVs phase-folded to the ephemeris of planet b with the orbit model of planet c subtracted. Red circles are the same velocities binned in 0.08 units of orbital phase. **d)** RVs phase-folded to the ephemeris of planet c.

K2 data using a Gaussian process as this dataset showed periodicity at the stellar rotation period; the posteriors of this fit are: $\gamma_{K2} = 3633710^{+190}_{-200}$ e$^-$s^{-1}, $\sigma_{K2} = 117^{+16}_{-15}$ e$^-$s^{-1}, $\eta_1 = 655^{+84}_{-68}$ e$^-$s^{-1}, $\eta_2 = 5.17^{+0.66}_{-0.64}$ days, $\eta_3 = 4.49^{+0.61}_{-0.26}$ days, $\eta_4 = 0.55^{+0.04}_{-0.044}$. We then performed a Gaussian process fit on the radial velocity data including priors on η_2, η_3, and η_4 from the K2 fit posteriors. This fit results in semi-amplitudes consistent to 1σ for both planets: the full results are shown in Table 5. The Gaussian process fit has a higher AIC value (ΔAIC=7.38) suggesting that Gaussian process parameters do not significantly improve the fit. For this reason, and as we do not see signs of stellar activity in our activity indicators or radial velocity data, we adopt the fit without a Gaussian process.

5.3. *Eccentricity Constraints*

We explored the range of planet eccentricities consistent with system stability through N-body simulations as including eccentricity was not warranted in our radial velocity fits for either system. The literature papers on GJ 9827 assumed circular orbits for their fits (Prieto-Arranz et al. 2018; Rice et al. 2019). For HD 106315, Barros et al. (2017) includes eccentricity terms in their radial velocity analysis resulting in e_b=0.1±0.1 and e_c=0.22±0.15, although they do not discuss if including the eccentricity terms improve the fit. Our eccentric radial velocity fit for HD 106315 resulted in e_b=0.18±0.17 and e_c=0.21±0.24, consistent with Barros et al. (2017). Though our eccentric fit had a higher AIC than the circular fit (ΔAIC=6.22) suggesting that including eccentricity did not sufficiently improve the fit to justify the additional parameters.

We evaluated the stability of both systems using `spock` (Tamayo et al. 2020). `spock` predicts whether a given orbital configuration is stable by using `rebound` (Rein & Liu 2011) to simulate the first 10^4 orbits of a system and then calculating the probability that this system is stable for a full 10^9 orbits by comparing it to a wide sample of full simulations. These full simulations include mean-motion resonance, mutually inclined, and eccentric systems; the parameters are drawn from those typically encountered in current multiplanet systems.

We initialized both systems at the maximum likelihood values for the planet masses, orbital periods, times of conjunction, and stellar masses derived in this paper.

We then varied e and ω for all planets to explore the stability of the system. For HD 106315, we varied e_1 and e_2 from 0.0 to 0.9 in steps of 0.1. At each eccentricity pair, we performed a grid of simulations varying ω_1 and ω_2 from 0 to 2π in steps of $\frac{\pi}{5}$, resulting in 10,000 simulations. We then averaged over the simulated ω grid to calculate the average probability that a given eccentricity pair is stable (Figure 7).

HD 106315 b and HD 106315 c are in relatively close orbits at periods of 9.55 and 21.06 days; their orbits are unstable if either planet has a large eccentricity. The system has a probability of stability greater than 50% when $e_1 \leq 0.4$ and $e_2 \leq 0.3$; the highest probability of stability is when both planets are in circular orbits.

GJ 9827 b, GJ 9827 c, and GJ 9827 d are in even more closely-packed orbits at orbital periods of 1.2, 3.6, and 6.2 days. Therefore, for GJ 9827, we varied e_1, e_2, and e_3 from 0.0 to 0.4 in steps of 0.1 as larger eccentricities for any of the three planets resulted in unstable orbits.

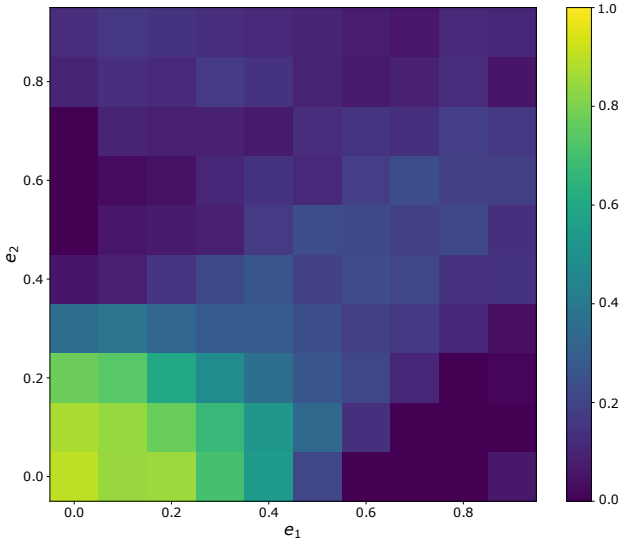

Figure 7. Probability of stability for the HD 106315 system. We examined the effect of planet eccentricity on the system's stability using `spock`. For each pair of eccentricities, we vary ω_1 and ω_2 from 0 to 2π. The color of the box displays the average probability of stability across all ω.

At each eccentricity triplet we perform a grid of simulations varying ω_1, ω_2, and ω_3 from 0 to 2π in steps of $\frac{\pi}{5}$, creating a total of 125,000 simulations. We then averaged over the ω grid to calculate the average probability that a given eccentricity triplet is stable (Figure 8).

We find that the GJ 9827 system is unstable if $e_3 \geq 0.3$ and the system has very low stability at $e_3 = 0.2$. For $e_3 \leq 0.1$, the system can be stable with $e_2 \leq 0.2$ and $e_1 \leq 0.4$. This system has a smaller range of stable eccentricity values since the planets are packed closer together.

We then convert these eccentricity constraints to secondary eclipse timing constraints (Winn 2010, equation 33). We note that the planets in these two systems are not particularly favorable targets for thermal emission spectroscopy based on the emission spectroscopy metric (ESM, Kempton et al. 2018, HD 106315 b: 3, HD 106315 c: 6, GJ 9827 b: 14, GJ 9827 c: 4, GJ 9827 d: 6).

From our eccentricity constraints and assuming ω=0, the maximum offsets of the secondary eclipse time for HD 106315 b and HD 106315 c are 2.4 days and 4.0 days respectively. The maximum secondary eclipse timing offsets for the GJ 9827 system are 0.31 days, 0.46 days, and 0.39 days for planet b, c, and d respectively.

6. INTERIOR BULK COMPOSITIONS

To explore the interior compositions of these planets, we first visually compare their masses and radii to other known exoplanets on a mass-radius diagram (Figure 9). GJ 9827 b (ρ_b=7.5 g cm^{-3}) and GJ 9827 c (ρ_c=6.1 g cm^{-3}) are both consistent with a 50/50 mixture of rock and iron. GJ 9827 d (ρ_d=2.5 g cm^{-3}) and HD 106315 b (ρ_b=4.1 g cm^{-3}) are consistent with either 100% water or a rocky core with a 1% H/He envelope. Lastly, HD 106315 c (ρ_c=0.8 g cm^{-3}) is located near our solar system ice giant planets. It has a much lower density than HD 106315 b, too low to be explained by water alone, and is consistent with having a >10% H/He envelope.

To further investigate the interior compositions of these planets, we compared their masses and radii with model composition grids from Zeng & Sasselov (2013); Lopez & Fortney (2014); Zeng et al. (2016). We focus on two main compositions: Earth-like rock & iron cores surrounded by H/He envelopes and mixtures of water, rock, and iron. Our results are tabulated in Table 6.

To calculate potential H/He mass fractions, we use the grids of thermal evolution models provided by Lopez & Fortney (2014) which calculate the radius of a planet given varying incident fluxes relative to Earth ($S_{inc}/S_\oplus$), masses ($M_p/M_\oplus$), ages, and fractions f_{HHe} of their masses contained in H/He envelopes surrounding Earth-like rock and iron cores. We use the `smint` (Structure Model INTerpolator) interpolation and envelope mass fraction fitting package, which we made publicly-available on GitHub[3], in order to solve the inverse problem of inferring a planet's envelope mass fraction from its incident flux, mass, age, and radius.

`smint` performs linear interpolation over a grid of f_{HHe}, $\log_{10} M_p/M_\oplus$, system age and $\log_{10} S_{inc}/S_\oplus$ and returns the corresponding planet radius. We then run a MCMC that fits for the combination of S_{inc}, M_p, age, and f_{HHe} that best matches the observed planet radius. We adopt Gaussian priors on S_{inc} and M_p informed by the stellar and planetary parameters. We use a uni-

Table 6. Hydrogen/Helium and Water Mass Fraction Surrounding an Earth-like Core

Planet	f_{HHe} (%)	f_{H_2O} (%)
GJ 9827b	$0.02^{+0.01}_{-0.01}$	$2.20^{+3.84}_{-1.69}$
GJ 9827c	$0.01^{+0.01}_{-0.00}$	$13.57^{+25.18}_{-10.40}$
GJ 9827d	$0.54^{+0.20}_{-0.17}$	$79.10^{+14.35}_{-20.14}$
HD 106315b	$0.96^{+0.72}_{-0.51}$	$54.29^{+29.06}_{-30.09}$
HD 106315c	$12.74^{+1.11}_{-1.06}$	$99.27^{+0.57}_{-1.25}$

[3] https://github.com/cpiaulet/smint

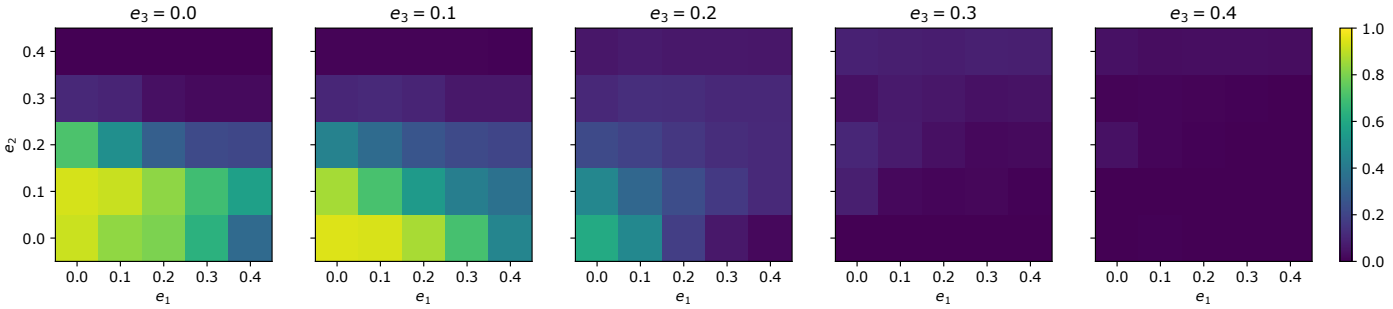

Figure 8. Probability of stability for the GJ 9827 system. We examined the effect of planet eccentricity on the system's stability using `spock`. For each triplet of eccentricities, we vary ω_1, ω_2, and ω_3 from 0 to 2π. The color of the box displays the average probability of stability across all ω.

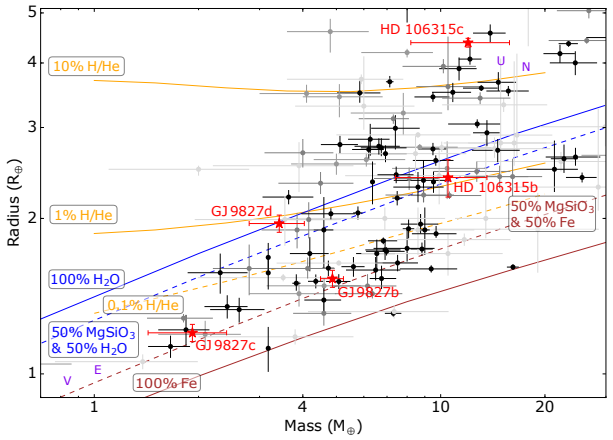

Figure 9. Mass-radius diagram for planets between the size of Earth and Neptune with greater than 2σ measurements (darker points for lower error). The lines show models of different compositions (Lopez & Fortney 2014; Zeng et al. 2016). Our five planets are shown as red stars with 1σ uncertainties.

form prior on the planet's envelope mass fraction over the range spanned by the Lopez & Fortney (2014) grids (from 0.1 to 20%) and adopt a uniform prior on the system age from 1 to 10 Gyr. Each of the 100 chains is run for at least 10,000 steps, 60% of which are discarded as burn-in. We make sure that, in each case, the chains have run for at least 50 times the maximum autocorrelation time recorded across all parameters and thus secure that our chains are converged and well sample the posterior PDFs. We display a corner plot for the three planets consistent with moderate H/He envelopes, GJ 9827 d, HD 106315 b, and HD 106315 c (Figure 10). GJ 9827 d and HD 106315 b are both consistent with 1% H/He envelopes and HD 106315 c is consistent with a 13% H/He envelope.

To fit for the water mass fractions (f_{H_2O}), we use the implementation of the Zeng et al. (2016) two-component (water+rock) model grid in `smint` (Table 6). The MCMC process is analog to that used to fit for f_{HHe}, adopting a uniform prior on the water mass fraction (0–100 %) and a Gaussian prior on the planet mass. We match the observed planet radius via a Gaussian likelihood.

To further investigate the potential f_{H_2O}, we explore three component models of H_2O, $MgSiO_3$, and Fe for four of our planets, excluding HD 106315 c as its low density is inconsistent with these models. We use a numerical tool[4] in order to solve for the interior structure of each planet and produce ternary diagrams of the range of combinations of $MgSiO_3$, Fe, and H_2O mass fractions that are compatible with the observed mass and radius (Zeng & Sasselov 2013; Zeng et al. 2016). These ternary diagrams are shown in Figure 11. GJ 9827 b and GJ 9827 c both have a low H_2O fraction ($\leq$40%) and a wide range of possibilities for $MgSiO_3$ & Fe. GJ 9827 d is consistent with a high H_2O fraction (50–100%) and small fractions of $MgSiO_3$ (0–50%) and Fe (0–30%). HD 106315 b is consistent with a wide range for all three components (10–100% H_2O, 0–90% $MgSiO_3$, and 0–60% Fe).

Both Prieto-Arranz et al. (2018) and Rice et al. (2019) suggest that photoevaporation may have sculpted the inner two rocky GJ 9827 planets. However, the outer planet, GJ 9827 d, must have retained a moderate fraction of volatiles to be consistent with its mass and radius. We examine whether the system as a whole is consistent with the theory of photoevaporation through calculating the minimum mass required of planet d to retain its atmosphere assuming planets b and c lost theirs to photoevaporation, as described in Owen & Campos Estrada (2019). We find the minimum mass for GJ 9827 d is 1 $M_\oplus$, lower than its mass of 3.3 $M_\oplus$. Therefore, this system is in agreement with this photoevaporation model (Owen & Wu 2013, 2017). Although,

[4] https://www.cfa.harvard.edu/~lzeng

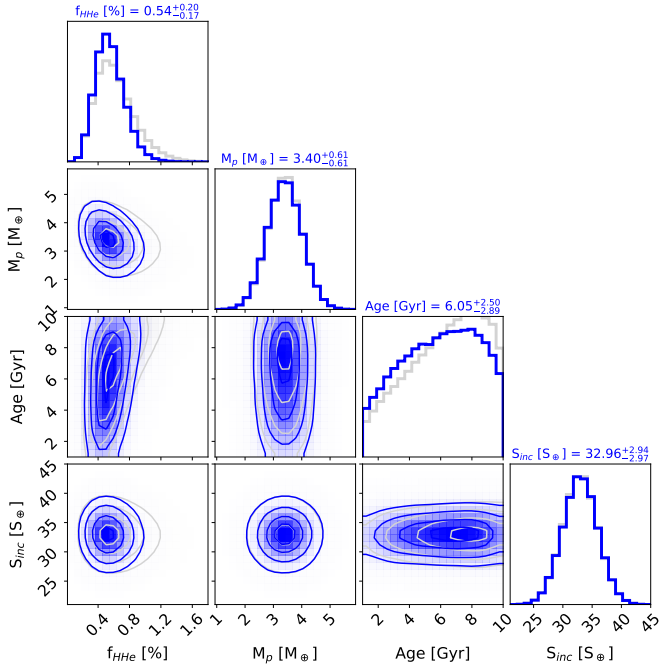

(a) GJ 9827 d

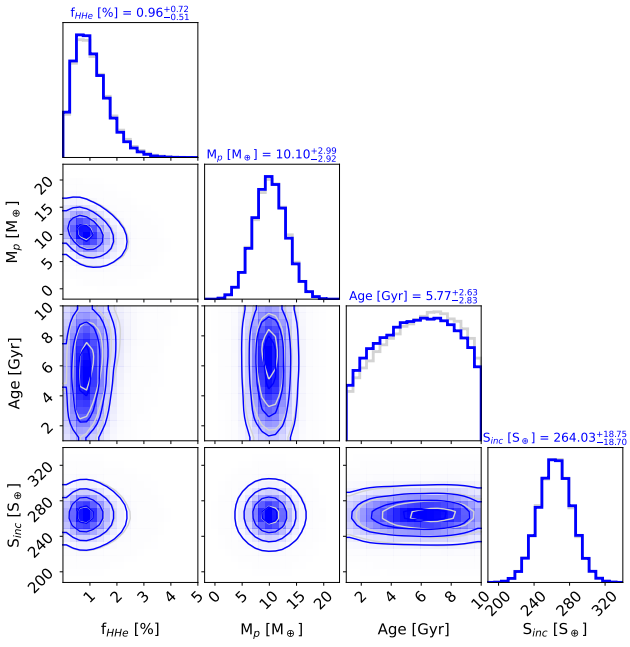

(b) HD 106315 b

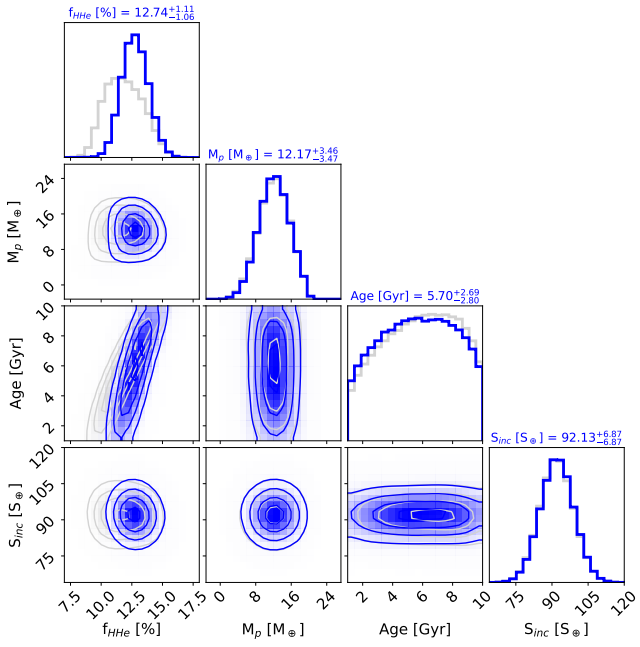

(c) HD 106315 c

Figure 10. Joint and marginalized posterior distributions on the fitted parameters for a 1× (50×) solar metallicity H_2/He envelope atop an Earth-like core are shown in blue (gray). The median and $\pm1\sigma$ constraints on the parameters for the 1× solar metallicity case are quoted above each marginalized distribution.

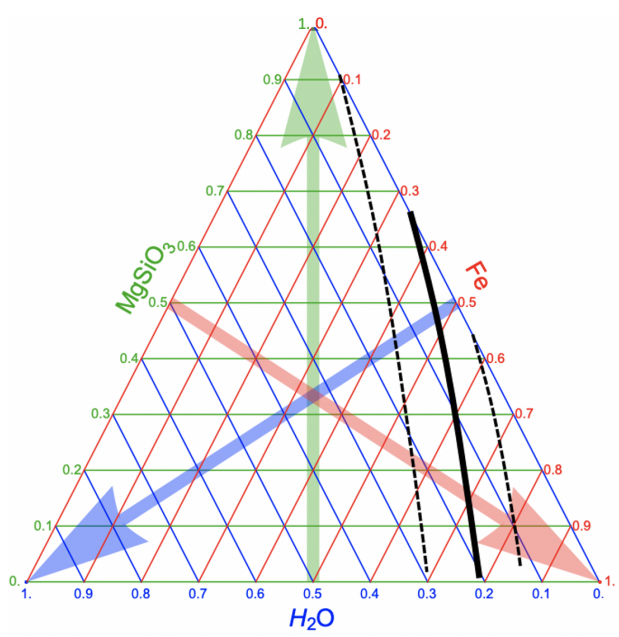

(a) GJ 9827 b

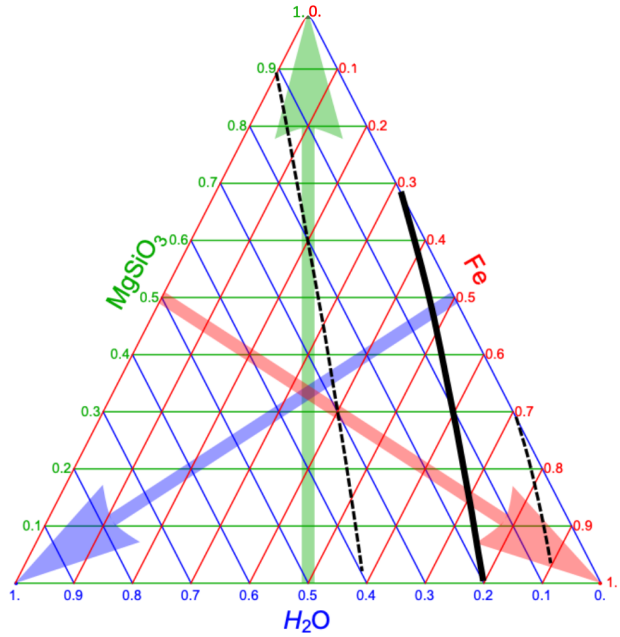

(b) GJ 9827 c

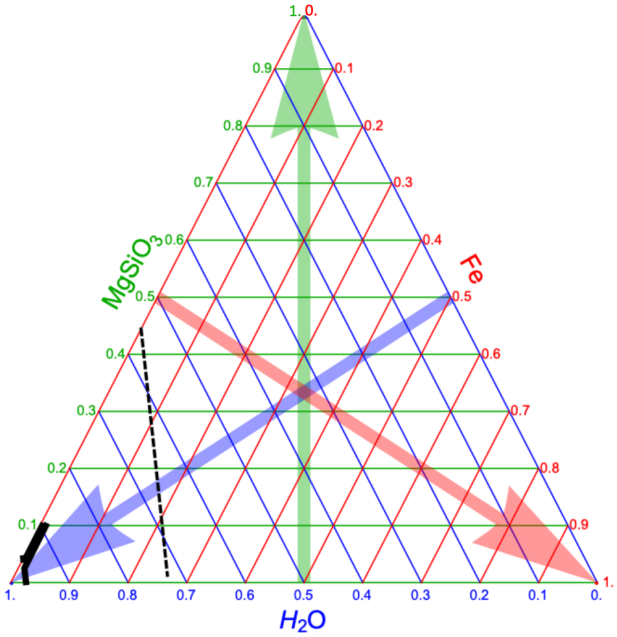

(c) GJ 9827 d

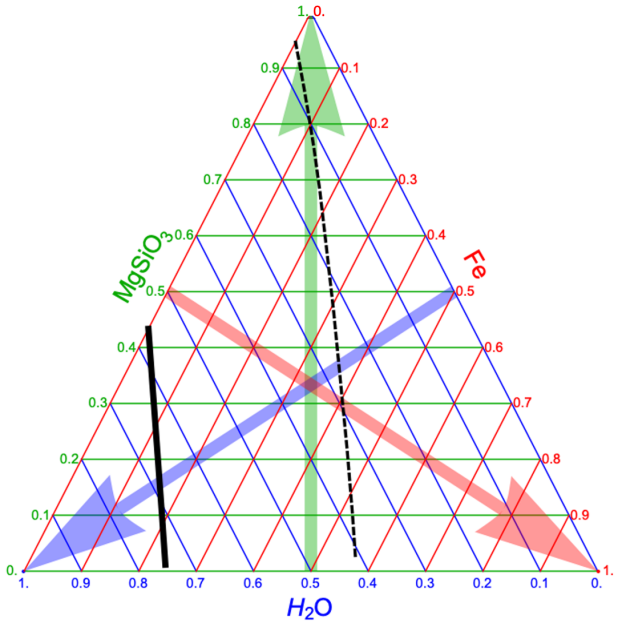

(d) HD 106315 b

Figure 11. Ternary diagrams using a 3-component H_2O/$MgSiO_3$/Fe model (Zeng & Sasselov 2013; Zeng et al. 2016). The solid line outlines the median mass and radius of each planet, while the dashed line(s) delineate the 1σ contours. At any point in the diagram the mass fractions can be found by following the three thin colored lines towards their respective side.

GJ 9827 d may have had a different type of atmospheric evolution other than photoevaporation. Kasper et al. (2020) set stringent limits on the presence of any extended atmosphere around GJ 9827 d via high-resolution spectroscopy of the metastable 10,833 Å He triplet, inconsistent with current models of atmospheric formation and mass loss.

Furthermore, the three GJ 9827 planets span the radius gap at $1.7R_\oplus$ (Fulton et al. 2017). The inner two planets are high density and smaller than the radius gap (R_b=$1.5R_\oplus$, R_c=$1.2R_\oplus$) whereas the outer planet is lower density and larger than the radius gap (R_d=$2.0R_\oplus$). HD 106315 b and c are both lower density and larger than the radius gap (R_b=$2.4R_\oplus$, R_c=$4.4R_\oplus$). The five planets in these systems agree with a theory that planets smaller than $1.7R_\oplus$ are primarily composed of rocky cores and larger planets have additional volatile material that contributes to their radii (Weiss et al. 2016; Fulton et al. 2017).

7. CONCLUSION

In this paper, we characterized two systems, HD 106315 and GJ 9827. These bright stars host super-Earth and sub-Neptune planets well suited for atmospheric characterization by HST and JWST. From our Spitzer analysis (Section 2) we improved the planets' ephemerides, enabling accurate transit prediction required for future atmospheric characterization through transmission spectroscopy. We incorporated Gaia parallaxes to update the stellar parameters for both systems and further constrained the limiting magnitude of nearby companions to HD 106315 through imaging data (Section 3).

As the results of a multi-year high-cadence observing campaign with Keck/HIRES and Magellan/PFS, we improved the planets' mass measurements in preparation for the interpretation of HST transmission spectra. We measured planet masses in the GJ 9827 system to be M_b=4.87 ± 0.37 $M_\oplus$, M_c=1.92 ± 0.49 $M_\oplus$, and M_d=3.42 ± 0.62 $M_\oplus$. For HD 106315, we found planet masses of M_b=10.5 ± 3.1 $M_\oplus$ and M_c=12.0 ± 3.8 $M_\oplus$. Atmospheric characterization of small planets benefits from mass detections at 5σ significance (Batalha et al. 2019). We have achieved 5σ masses for two planets with pending HST analyses, GJ 9827 b and GJ 9827 d (Hedges et al. in prep, Benneke et al in prep), and a 4σ mass for the third, HD 106315 c (Kreidberg et al. 2020).

For GJ 9827, stellar activity signatures in the photometry and Calcium II H&K lines (Section 4) informed our use of a Gaussian process to account for this activity in our radial velocity fit. We did not adopt the Gaussian process fit for our HD 106315 analysis due to the higher AIC value and the lack of activity signatures seen in the Calcium II H&K lines and radial velocity data. Hotter stars ($T_{\rm eff}$ >6200 K) often have shallow convective envelopes and inefficient magnetic dynamos which result in fewer spots on the stellar surface (Kraft 1967). Therefore, hotter stars like HD 106315 may not have enough starspots for this type of Gaussian process to be effective.

We additionally explored the possible eccentricities for these planets through stability arguments. We found that low eccentricities are required for stability for these two closely-packed systems. We finally compared our derived masses and densities with previously published models to investigate interior compositions for these planets. We found GJ 9827 b and GJ 9827 c are both consistent with a 50/50 rock-iron composition, GJ 9827 d and HD 106315 b both require additional volatiles, and HD 106315 c is consistent with a ∼10% by mass hydrogen/helium envelope.

8. APPENDIX

Table 7. GJ 9827 Radial Velocities

Time (BJD_{TDB})	RV (m s^{-1})	RV Unc. (m s^{-1})	S_{HK}	H-alpha	Instrument
2458787.89755	4.67	1.16	0.5741	0.05581	HIRES
2458118.80405	-0.01	1.08	0.7945	0.05629	HIRES
2458646.10457	0.93	0.98	0.6726	0.05624	HIRES
2458776.89384	-4.37	1.61	0.5287	0.05622	HIRES
2458125.76818	-9.47	1.20	0.7162	0.05662	HIRES
2458324.04450	-1.40	1.22	0.6486	0.05680	HIRES

Table 7 *continued*

Table 7 *(continued)*

Time (BJD_{TDB})	RV (m s^{-1})	RV Unc. (m s^{-1})	S_{HK}	H-alpha	Instrument
2458300.01918	-10.13	1.26	0.7221	0.05711	HIRES
2458391.98260	-13.69	1.21	0.6795	0.05708	HIRES
2458476.72361	-9.02	1.07	0.7117	0.05646	HIRES
2458341.05653	-4.39	1.14	0.6928	0.05671	HIRES
2458264.10151	-4.81	1.04	0.6822	0.05618	HIRES
2458663.09765	1.91	1.04	0.6394	0.05695	HIRES
2458361.06735	-0.48	1.15	0.6929	0.05552	HIRES
2458018.89464	4.00	1.14	0.6342	0.05697	HIRES
2458462.76041	3.12	1.07	0.7086	0.05636	HIRES
2458345.11938	0.04	1.46	0.6418	0.05576	HIRES
2458285.11926	0.87	1.18	0.6411	0.05655	HIRES
2458019.90188	-4.03	1.13	0.6190	0.05611	HIRES
2458724.91297	-0.24	1.16	0.5269	0.05645	HIRES
2458716.08123	-4.38	1.30	0.5279	0.05626	HIRES
2458396.85939	-0.81	1.11	0.6396	0.05751	HIRES
2458389.01961	-0.55	1.40	0.6611	0.05627	HIRES
2458346.10048	-2.88	1.21	0.6692	0.05640	HIRES
2458662.08768	0.41	1.02	0.6354	0.05657	HIRES
2458724.02187	-1.99	1.07	0.5176	0.05619	HIRES
2458395.95532	3.94	1.01	0.6920	0.05704	HIRES
2458124.79535	-7.35	1.53	0.7996	0.05669	HIRES
2458746.98946	0.61	1.06	0.5388	0.05542	HIRES
2458709.89709	-14.83	1.23	0.5539	0.05526	HIRES
2458443.86005	-7.99	1.11	0.7280	0.05749	HIRES
2458295.07494	0.69	1.07	0.6887	0.05646	HIRES
2458265.11117	-7.06	1.29	0.6877	0.05642	HIRES
2458733.03468	-3.91	1.09	0.5733	0.05525	HIRES
2458723.08397	-9.46	1.26	0.5221	0.05615	HIRES
2458436.77435	-6.51	1.11	–	0.05671	HIRES
2458299.10180	-4.48	1.19	0.7032	0.05699	HIRES
2458091.81565	4.65	1.17	0.8633	0.05655	HIRES
2458833.76746	-2.47	1.16	0.5241	0.05508	HIRES
2458393.94943	-2.99	1.19	0.6665	0.05718	HIRES
2458383.99765	4.71	1.24	0.6485	0.05708	HIRES
2458309.01867	-4.57	1.12	0.7225	0.05698	HIRES
2458680.01498	-6.33	1.08	0.6814	0.05561	HIRES
2458832.81639	0.24	1.12	0.5802	0.05560	HIRES
2458652.11022	-3.33	1.07	0.6355	0.05712	HIRES
2458370.03794	-1.95	1.14	0.7151	0.05705	HIRES
2458490.70951	-1.38	1.25	0.7028	0.05679	HIRES

Table 7 *continued*

Table 7 *(continued)*

Time (BJD_{TDB})	RV (m s^{-1})	RV Unc. (m s^{-1})	S_{HK}	H-alpha	Instrument
2458350.05809	3.53	1.31	0.6635	0.05667	HIRES
2458116.71383	4.52	1.08	0.6439	0.05704	HIRES
2458293.10940	-1.28	1.13	0.6735	0.05647	HIRES
2458651.10778	0.07	1.03	0.6294	0.05590	HIRES
2458802.84282	-6.52	1.25	0.5617	0.05507	HIRES
2458737.90776	-5.52	1.11	0.5445	0.05570	HIRES
2458364.04552	-7.36	1.14	0.7050	0.05531	HIRES
2458387.97876	1.60	1.08	0.6494	0.05737	HIRES
2458844.80960	1.47	1.06	0.5513	0.05582	HIRES
2458856.74435	-6.18	1.46	0.5642	0.05665	HIRES
2458827.80197	-1.10	0.99	0.5579	0.03639	HIRES
2458337.10349	-0.30	1.15	0.7241	0.05619	HIRES
2458715.07051	0.56	1.11	0.5301	0.05594	HIRES
2458024.02110	-1.63	1.34	0.6228	0.05587	HIRES
2458491.71209	-0.28	1.02	0.7160	0.05646	HIRES
2458117.80128	4.23	1.07	0.7354	0.05637	HIRES
2458306.03964	-3.06	1.15	0.7271	0.05795	HIRES
2458739.06355	-4.30	1.18	0.5273	0.05488	HIRES
2458099.72693	-3.67	1.17	0.6767	0.05645	HIRES
2458855.74402	-10.15	1.39	0.5894	0.05608	HIRES
2458845.75181	1.34	1.11	0.5558	0.05581	HIRES
2458647.11328	-9.14	0.93	0.6622	0.05659	HIRES
2458819.83041	0.87	1.26	0.5522	0.05540	HIRES
2458392.97702	-7.79	1.11	0.6593	0.05694	HIRES
2458328.93752	-4.21	1.31	0.6909	0.05687	HIRES
2458351.07086	1.74	1.35	0.6618	0.05672	HIRES
2458329.99590	-1.30	1.20	0.7188	0.05677	HIRES
2458815.82726	0.04	1.13	0.5760	0.05550	HIRES
2458324.95128	4.55	1.25	0.6582	0.05667	HIRES
2458720.07172	2.33	1.33	0.5106	0.05586	HIRES
2458367.01976	3.63	1.36	0.7497	0.05757	HIRES
2458149.72124	7.73	1.23	0.8321	0.05668	HIRES
2458797.92260	-6.80	1.17	0.5685	0.05540	HIRES
2458097.78803	2.71	1.13	0.6741	0.05631	HIRES
2458291.10956	-0.65	0.96	0.6571	0.05603	HIRES
2458296.04279	7.36	0.97	0.7101	0.05693	HIRES
2458338.10518	2.52	1.25	0.7101	0.05613	HIRES
2458098.81794	7.06	1.17	0.6766	0.05621	HIRES
2458389.98455	-0.19	1.21	0.6644	0.05592	HIRES
2458267.11611	6.21	1.11	0.6743	0.05696	HIRES

Table 7 *continued*

Table 7 *(continued)*

Time (BJD_{TDB})	RV (m s^{-1})	RV Unc. (m s^{-1})	S_{HK}	H-alpha	Instrument
2458292.10445	-0.10	0.99	0.6650	0.05657	HIRES
2458301.00170	-9.07	1.26	0.7224	0.05679	HIRES
2458366.10026	1.07	1.27	0.7132	0.05513	HIRES
2458327.93655	-5.02	1.23	0.6860	0.05686	HIRES
2458266.11293	6.35	1.13	0.6764	0.05652	HIRES
2458020.90394	-7.94	1.13	0.6277	0.05662	HIRES

HIRES S_{HK} values have an uncertainty of 0.001.

Table 8. HD 106315 Radial Velocities

Time (BJD_{TDB})	RV (m s^{-1})	RV Unc. (m s^{-1})	S_{HK}	H-alpha	Instrument
2457746.13882	-6.58	4.11	0.1392	0.03299	HIRES
2457746.14353	-3.36	4.01	0.1391	0.03294	HIRES
2457747.06934	0.11	3.79	0.1398	0.03288	HIRES
2457747.10551	1.64	4.17	0.1399	0.03321	HIRES
2457747.15981	15.16	3.95	0.1404	0.03313	HIRES
2457760.09582	2.62	4.15	0.1369	0.03307	HIRES
2457760.13104	-13.59	3.97	0.1375	0.03306	HIRES
2457760.17348	-7.50	4.13	0.1398	0.03304	HIRES
2457764.01751	6.98	4.29	0.1374	0.03304	HIRES
2457764.05279	1.81	4.50	0.1386	0.03283	HIRES
2457764.09032	2.78	4.01	0.1395	0.03307	HIRES
2457764.09369	3.45	3.94	0.1392	0.03305	HIRES
2457764.09704	8.54	3.92	0.1390	0.03305	HIRES
2457764.13272	-10.27	4.58	0.1396	0.03316	HIRES
2457764.17257	5.27	3.83	0.1386	0.03320	HIRES
2457765.02368	-10.26	3.91	0.1387	0.03288	HIRES
2457765.02889	-6.80	4.20	0.1382	0.03293	HIRES
2457765.03277	-5.33	4.16	0.1389	0.03288	HIRES
2457765.06829	-7.55	3.94	0.1382	0.03296	HIRES
2457765.14462	-1.96	3.95	0.1379	0.03316	HIRES
2457765.15150	-7.33	4.13	0.1386	0.03325	HIRES
2457765.15892	-0.70	4.17	0.1380	0.03313	HIRES
2457766.02041	0.03	4.10	0.1356	0.03301	HIRES
2457766.05479	-15.51	4.32	0.1362	0.03296	HIRES
2457766.10347	-17.81	4.16	0.1371	0.03334	HIRES
2457766.13313	-12.24	4.04	0.1371	0.03325	HIRES

Table 8 *continued*

Table 8 *(continued)*

Time (BJD_{TDB})	RV (m s^{-1})	RV Unc. (m s^{-1})	S_{HK}	H-alpha	Instrument
2457766.17504	-16.04	4.19	0.1364	0.03330	HIRES
2457775.00337	-18.93	5.04	0.1395	0.03277	HIRES
2457775.08336	-7.43	5.14	0.1382	0.03290	HIRES
2457775.14543	15.95	5.16	0.1386	0.03290	HIRES
2457775.17945	13.34	5.29	0.1318	0.03282	HIRES
2457775.97301	6.76	5.29	0.1366	0.03331	HIRES
2457776.03370	-0.88	5.29	0.1371	0.03312	HIRES
2457776.07307	-3.10	5.30	0.1377	0.03291	HIRES
2457776.11667	-0.40	5.40	0.1358	0.03291	HIRES
2457776.17591	9.27	4.93	0.1350	0.03307	HIRES
2457788.03576	-6.97	5.33	0.1337	0.03292	HIRES
2457788.09236	-8.83	5.18	0.1353	0.03288	HIRES
2457788.14459	10.39	5.43	0.1361	0.03276	HIRES
2457788.96764	-1.52	4.97	0.1368	0.03274	HIRES
2457789.03425	-11.90	5.20	0.1358	0.03308	HIRES
2457789.07579	-16.63	4.92	0.1356	0.03296	HIRES
2457789.12552	-1.69	4.93	0.1309	0.03305	HIRES
2457789.93588	-14.19	5.35	0.1372	0.03276	HIRES
2457789.97055	-6.69	5.46	0.1371	0.03302	HIRES
2457790.02625	10.37	4.80	0.1380	0.03304	HIRES
2457790.07667	11.05	5.24	0.1374	0.03305	HIRES
2457790.11637	-0.66	5.88	0.1375	0.03307	HIRES
2457790.94126	3.04	4.48	0.1340	0.03293	HIRES
2457790.98855	3.61	4.85	0.1321	0.03305	HIRES
2457791.02903	3.53	4.62	0.1304	0.03301	HIRES
2457791.06239	3.40	4.51	0.1316	0.03311	HIRES
2457791.13144	-5.63	4.45	0.1331	0.03314	HIRES
2457792.95306	5.29	4.31	0.1331	0.03268	HIRES
2457793.01216	1.33	4.48	0.1349	0.03287	HIRES
2457793.06477	-1.47	4.64	0.1353	0.03306	HIRES
2457793.09752	7.74	5.09	0.1331	0.03315	HIRES
2457794.01892	-1.13	4.53	0.1361	0.03299	HIRES
2457794.06873	9.90	4.53	0.1362	0.03300	HIRES
2457794.12856	-9.77	4.72	0.1354	0.03300	HIRES
2457794.96285	2.04	4.70	0.1356	0.03299	HIRES
2457795.00019	14.61	4.38	0.1358	0.03312	HIRES
2457795.11828	3.57	4.55	0.1356	0.03295	HIRES
2457796.00198	17.72	5.51	0.1333	0.03305	HIRES
2457802.91637	-1.14	4.26	0.1358	0.03303	HIRES
2457802.94277	0.19	4.26	0.1354	0.03316	HIRES

Table 8 *continued*

Table 8 *(continued)*

Time (BJD_{TDB})	RV (m s^{-1})	RV Unc. (m s^{-1})	S_{HK}	H-alpha	Instrument
2457803.89893	-10.62	4.28	0.1332	0.03302	HIRES
2457803.92126	-5.97	4.48	0.1356	0.03288	HIRES
2457804.89453	1.83	8.27	0.1174	0.03349	HIRES
2457805.87966	-16.14	4.06	0.1360	0.03259	HIRES
2457805.91546	3.79	4.77	0.1385	0.03309	HIRES
2457805.94644	-16.41	5.74	0.1370	0.03288	HIRES
2457806.87926	0.21	5.35	0.1304	0.03285	HIRES
2457806.91553	-7.60	4.51	0.1348	0.03298	HIRES
2457806.96445	-8.99	4.41	0.1355	0.03353	HIRES
2457828.91583	-15.48	4.56	0.1359	0.03302	HIRES
2457828.97000	-1.71	4.68	0.1355	0.03307	HIRES
2457829.04172	-10.00	4.83	0.1359	0.03298	HIRES
2457829.83091	-9.99	4.62	0.1350	0.03283	HIRES
2457829.94218	-16.57	4.63	0.1343	0.03296	HIRES
2457830.05077	-9.15	4.37	0.1360	0.03296	HIRES
2457830.95834	3.17	4.85	0.1376	0.03369	HIRES
2457830.97649	-11.76	4.62	0.1373	0.03382	HIRES
2457831.02642	-13.07	4.52	0.1364	0.03318	HIRES
2457886.92496	-11.37	3.97	0.1365	0.03352	HIRES
2457887.94831	-11.08	4.43	0.1361	0.03325	HIRES
2457887.97540	-4.90	4.18	0.1324	0.03308	HIRES
2457925.75207	2.27	4.26	0.1332	0.03285	HIRES
2457925.75570	-0.51	3.95	0.1340	0.03281	HIRES
2457925.75951	-5.71	4.27	0.1336	0.03282	HIRES
2457925.84733	-5.79	3.96	0.1355	0.03266	HIRES
2457925.85224	6.53	3.72	0.1351	0.03262	HIRES
2457925.85715	-11.74	4.20	0.1351	0.03268	HIRES
2457925.87848	2.19	4.05	0.1353	0.03260	HIRES
2457926.75519	5.55	4.06	0.1362	0.03313	HIRES
2457926.75814	0.27	4.01	0.1356	0.03312	HIRES
2457926.76117	4.34	4.36	0.1359	0.03312	HIRES
2457926.81714	-3.79	4.44	0.1351	0.03279	HIRES
2457926.82071	-6.63	4.53	0.1351	0.03279	HIRES
2457926.82430	-6.60	4.53	0.1351	0.03284	HIRES
2457926.87381	1.71	4.09	0.1351	0.03257	HIRES
2457926.87805	-13.30	4.41	0.1349	0.03260	HIRES
2457926.88191	-12.34	4.85	0.1349	0.03266	HIRES
2457932.74875	-15.49	4.25	0.1338	0.03287	HIRES
2457932.75265	-7.25	4.22	0.1334	0.03286	HIRES
2457932.75644	-7.54	4.53	0.1337	0.03304	HIRES

Table 8 *continued*

Table 8 *(continued)*

Time (BJD_{TDB})	RV (m s^{-1})	RV Unc. (m s^{-1})	S_{HK}	H-alpha	Instrument
2457932.82664	-7.59	4.14	0.1327	0.03280	HIRES
2457932.83122	-20.21	4.66	0.1328	0.03282	HIRES
2457932.83577	2.63	4.09	0.1329	0.03278	HIRES
2457939.75845	2.40	4.46	0.1273	0.03304	HIRES
2457939.76412	4.70	4.70	0.1259	0.03309	HIRES
2457939.76959	3.76	4.65	0.1278	0.03301	HIRES
2457940.79054	6.71	4.28	0.1333	0.03268	HIRES
2457940.79493	-4.74	4.22	0.1321	0.03273	HIRES
2457940.79981	-6.94	4.08	0.1302	0.03280	HIRES
2457964.75862	-2.12	4.56	0.1350	0.03332	HIRES
2457964.76469	-1.59	4.59	0.1351	0.03317	HIRES
2458113.08369	-8.93	4.71	0.1360	0.03293	HIRES
2458113.09308	-8.40	4.12	0.1366	0.03296	HIRES
2458113.09715	-5.69	4.00	0.1362	0.03305	HIRES
2458114.03130	0.92	4.34	0.1372	0.03288	HIRES
2458114.03639	-11.77	4.31	0.1317	0.03292	HIRES
2458114.04179	-6.28	4.43	0.1341	0.03297	HIRES
2458114.08344	-7.93	4.44	0.1381	0.03321	HIRES
2458114.08768	-8.53	4.13	0.1372	0.03322	HIRES
2458114.09184	3.60	4.22	0.1381	0.03335	HIRES
2458149.95743	-7.48	4.10	0.1389	0.03304	HIRES
2458149.96341	-3.46	4.12	0.1379	0.03307	HIRES
2458149.96889	-4.02	4.30	0.1384	0.03307	HIRES
2458150.10402	-5.04	4.86	0.1271	0.03348	HIRES
2458150.11108	-2.19	4.73	0.1338	0.03365	HIRES
2458150.11674	-0.77	4.72	0.1351	0.03353	HIRES
2458150.93670	-5.13	4.53	0.1371	0.03294	HIRES
2458150.94605	-1.17	4.89	0.1380	0.03301	HIRES
2458150.95438	-8.99	4.76	0.1376	0.03298	HIRES
2458151.01303	5.26	4.34	0.1378	0.03314	HIRES
2458151.01794	4.91	4.90	0.1379	0.03306	HIRES
2458151.02280	3.30	4.11	0.1378	0.03315	HIRES
2458161.11153	1.27	4.29	0.1358	0.03284	HIRES
2458161.11535	-3.61	4.58	0.1364	0.03298	HIRES
2458161.11932	-14.38	4.54	0.1355	0.03291	HIRES
2458194.96586	3.35	5.03	0.1396	0.03343	HIRES
2458194.96962	0.96	4.92	0.1395	0.03331	HIRES
2458194.97338	5.12	4.76	0.1397	0.03339	HIRES
2458199.95986	-11.36	4.80	0.1371	0.04975	HIRES
2458247.95188	-0.95	4.39	0.1344	0.03361	HIRES

Table 8 *continued*

Table 8 *(continued)*

Time (BJD_{TDB})	RV (m s^{-1})	RV Unc. (m s^{-1})	S_{HK}	H-alpha	Instrument
2458247.98535	-6.99	4.91	0.1342	0.03202	HIRES
2458284.74670	-7.79	4.25	0.1378	0.03300	HIRES
2458284.75052	-7.46	4.53	0.1379	0.03303	HIRES
2458284.75435	-0.95	4.44	0.1388	0.03302	HIRES
2458294.75288	-12.54	4.11	0.1359	0.03314	HIRES
2458294.75633	-7.78	4.27	0.1359	0.03319	HIRES
2458294.75966	-5.97	4.18	0.1361	0.03320	HIRES
2458295.76177	-1.04	4.64	0.1347	0.03331	HIRES
2458295.76762	-4.38	3.85	0.1354	0.03329	HIRES
2458295.77317	-12.32	4.34	0.1362	0.03334	HIRES
2458298.76417	5.58	4.60	0.1363	0.03332	HIRES
2458298.76812	-4.93	4.35	0.1366	0.03328	HIRES
2458298.77221	0.53	4.39	0.1365	0.03322	HIRES
2458299.75015	-10.27	4.37	0.1376	0.03318	HIRES
2458299.75451	-2.26	4.75	0.1378	0.03316	HIRES
2458299.75887	-2.35	4.22	0.1379	0.03314	HIRES
2458300.76210	-7.52	4.50	0.1355	0.03318	HIRES
2458300.76556	-2.26	4.31	0.1360	0.03310	HIRES
2458300.76895	1.77	4.38	0.1355	0.03325	HIRES
2458301.77150	17.34	4.99	0.1389	0.03365	HIRES
2458303.74928	-4.68	4.28	0.1381	0.03305	HIRES
2458303.75263	1.69	4.24	0.1380	0.03304	HIRES
2458303.75621	3.79	4.03	0.1381	0.03306	HIRES
2458305.81046	-4.01	4.26	0.1355	0.03326	HIRES
2458305.81521	-9.77	4.32	0.1350	0.03319	HIRES
2458305.82007	-9.03	4.35	0.1346	0.03314	HIRES
2458307.77651	-13.55	4.72	0.1319	0.03310	HIRES
2458307.78206	-8.90	4.51	0.1336	0.03316	HIRES
2458307.78721	-16.93	4.61	0.1328	0.03301	HIRES
2458308.80024	-11.53	4.26	0.1346	0.03299	HIRES
2458308.80495	-15.77	4.50	0.1344	0.03271	HIRES
2458308.80947	-12.66	4.17	0.1344	0.03296	HIRES
2458323.75053	-11.87	4.18	0.1322	0.03295	HIRES
2458323.75826	-20.17	4.47	0.1286	0.03299	HIRES
2458323.76745	-2.81	4.71	0.1270	0.03299	HIRES
2458324.74711	-15.96	4.37	0.1347	0.03298	HIRES
2458324.75189	-14.12	4.39	0.1339	0.03306	HIRES
2458324.75797	-16.04	4.22	0.1338	0.03293	HIRES
2458491.06151	5.22	3.96	0.1398	0.03326	HIRES
2458491.06721	6.10	3.89	0.1400	0.03319	HIRES

Table 8 *continued*

Table 8 *(continued)*

Time (BJD_{TDB})	RV (m s^{-1})	RV Unc. (m s^{-1})	S_{HK}	H-alpha	Instrument
2458491.07267	-1.59	4.12	0.1394	0.03321	HIRES
2458491.12711	0.38	3.96	0.1389	0.03323	HIRES
2458491.13151	-1.88	3.92	0.1382	0.03319	HIRES
2458491.13662	0.09	3.95	0.1397	0.03314	HIRES
2458492.00757	0.56	3.90	0.1389	0.03308	HIRES
2458492.01111	8.38	4.13	0.1387	0.03305	HIRES
2458492.01468	-2.83	4.04	0.1392	0.03305	HIRES
2458492.07044	19.16	4.18	0.1387	0.03330	HIRES
2458492.07379	-3.72	3.81	0.1390	0.03335	HIRES
2458492.07719	-2.58	3.66	0.1384	0.03334	HIRES
2458492.12123	-3.90	4.32	0.1393	0.03341	HIRES
2458492.12472	8.06	4.02	0.1393	0.03335	HIRES
2458492.12820	5.37	4.12	0.1391	0.03340	HIRES
2458532.93369	9.71	4.16	0.1387	0.03312	HIRES
2458532.93872	-6.50	3.96	0.1382	0.03330	HIRES
2458532.94371	1.36	4.06	0.1376	0.03325	HIRES
2458533.00188	9.85	4.29	0.1381	0.03344	HIRES
2458533.00611	7.75	4.01	0.1376	0.03338	HIRES
2458533.01024	0.00	4.17	0.1373	0.03352	HIRES
2458533.06987	6.77	4.05	0.1378	0.03354	HIRES
2458533.07437	7.20	3.87	0.1379	0.03346	HIRES
2458533.07857	5.43	4.30	0.1385	0.03354	HIRES
2458559.86044	-14.59	4.66	0.1407	0.03359	HIRES
2458559.86545	-17.11	4.51	0.1406	0.03338	HIRES
2458559.86996	-17.09	4.38	0.1401	0.03353	HIRES
2458559.95743	-5.17	4.54	0.1402	0.03396	HIRES
2458559.96168	-9.94	4.42	0.1409	0.03391	HIRES
2458559.96622	-2.16	4.41	0.1401	0.03379	HIRES
2458560.01730	-1.43	4.56	0.1404	0.03373	HIRES
2458560.02263	-3.45	4.24	0.1403	0.03365	HIRES
2458560.02774	2.49	4.20	0.1402	0.03369	HIRES
2458566.95939	2.30	4.68	0.1372	0.03338	HIRES
2458566.96623	12.43	4.79	0.1372	0.03317	HIRES
2458566.97435	27.78	4.88	0.1368	0.03342	HIRES
2458567.02561	80.40	5.43	0.1383	0.03344	HIRES
2458567.04056	102.65	5.85	0.1380	0.03333	HIRES
2458567.04794	18.92	4.49	0.1367	0.03323	HIRES
2458568.81903	-6.03	4.33	0.1364	0.03310	HIRES
2458568.82355	6.29	4.42	0.1361	0.03316	HIRES
2458568.82793	1.12	4.82	0.1366	0.03312	HIRES

Table 8 *continued*

Table 8 *(continued)*

Time (BJD_{TDB})	RV (m s^{-1})	RV Unc. (m s^{-1})	S_{HK}	H-alpha	Instrument
2458568.91443	0.94	4.45	0.1358	0.03333	HIRES
2458568.91785	3.22	4.70	0.1361	0.03342	HIRES
2458568.92136	-8.03	4.37	0.1355	0.03332	HIRES
2458569.83303	12.47	4.63	0.1354	0.03323	HIRES
2458569.83678	21.89	4.50	0.1356	0.03320	HIRES
2458569.84071	0.70	4.49	0.1365	0.03308	HIRES
2458569.92580	12.24	4.55	0.1351	0.03326	HIRES
2458569.92944	12.05	4.39	0.1359	0.03329	HIRES
2458569.93329	3.50	4.61	0.1357	0.03326	HIRES
2458584.88918	4.05	4.72	0.1365	0.03332	HIRES
2458584.89615	-2.20	4.67	0.1366	0.03318	HIRES
2458584.90306	4.27	4.81	0.1365	0.03321	HIRES
2458592.95226	-22.65	4.52	0.1364	0.03323	HIRES
2458592.95676	-23.53	4.49	0.1365	0.03324	HIRES
2458592.96169	-46.04	4.53	0.1359	0.03325	HIRES
2458595.81757	4.50	4.60	0.1380	0.03305	HIRES
2458595.82100	-0.75	4.48	0.1376	0.03310	HIRES
2458595.82449	5.94	4.84	0.1380	0.03307	HIRES
2458595.87183	12.89	4.53	0.1376	0.03299	HIRES
2458595.87533	-17.78	4.92	0.1380	0.03295	HIRES
2458595.87873	3.46	4.92	0.1377	0.03302	HIRES
2458599.77326	-2.12	4.51	0.1366	0.03295	HIRES
2458599.77656	-6.93	4.55	0.1369	0.03310	HIRES
2458599.77994	-1.36	4.67	0.1363	0.03310	HIRES
2458610.86968	-0.13	4.48	0.1379	0.03272	HIRES
2458610.87354	7.16	4.34	0.1380	0.03264	HIRES
2458610.87724	3.72	4.14	0.1382	0.03284	HIRES
2458615.76217	-0.99	4.49	0.1374	0.03339	HIRES
2458615.76568	6.66	4.11	0.1381	0.03347	HIRES
2458615.76915	-0.59	4.24	0.1383	0.03333	HIRES
2458615.84636	8.56	4.32	0.1378	0.03364	HIRES
2458615.84979	1.18	4.49	0.1378	0.03375	HIRES
2458615.85320	-6.47	4.26	0.1378	0.03353	HIRES
2458616.83882	-5.61	3.96	0.1373	0.03290	HIRES
2458616.84231	-1.77	4.00	0.1376	0.03296	HIRES
2458616.84587	5.76	4.50	0.1370	0.03301	HIRES
2458616.89557	-4.15	4.05	0.1378	0.03308	HIRES
2458616.89872	6.75	4.13	0.1372	0.03305	HIRES
2458616.90188	7.06	4.05	0.1369	0.03330	HIRES
2458622.80874	-4.91	4.37	0.1373	0.03326	HIRES

Table 8 *continued*

Table 8 *(continued)*

Time (BJD_{TDB})	RV (m s^{-1})	RV Unc. (m s^{-1})	S_{HK}	H-alpha	Instrument
2458622.81217	-8.17	4.30	0.1376	0.03343	HIRES
2458622.81565	6.23	4.19	0.1376	0.03344	HIRES
2458622.88602	1.62	4.03	0.1364	0.03308	HIRES
2458622.89232	-5.79	4.14	0.1366	0.03342	HIRES
2458622.89780	-13.17	4.13	0.1368	0.03338	HIRES
2458623.74265	10.84	4.03	0.1350	0.03318	HIRES
2458623.74675	-1.11	4.46	0.1357	0.03338	HIRES
2458623.75081	11.45	4.33	0.1336	0.03342	HIRES
2458623.86571	-6.69	4.12	0.1369	0.03311	HIRES
2458623.87014	-4.93	4.09	0.1370	0.03307	HIRES
2458623.87500	-0.48	3.78	0.1370	0.03318	HIRES
2458627.74481	0.33	4.12	0.1366	0.03356	HIRES
2458627.74848	-12.67	4.34	0.1369	0.03367	HIRES
2458627.75218	-10.21	4.58	0.1374	0.03350	HIRES
2458627.84051	-9.14	4.17	0.1382	0.03331	HIRES
2458627.84511	-6.16	4.22	0.1383	0.03334	HIRES
2458627.84943	-9.02	4.20	0.1384	0.03330	HIRES
2458628.74062	-9.19	4.16	0.1349	0.03301	HIRES
2458628.74411	6.28	4.42	0.1362	0.03304	HIRES
2458628.74779	-7.19	4.28	0.1356	0.03308	HIRES
2458628.81257	-6.73	4.48	0.1374	0.03307	HIRES
2458628.81667	4.30	4.14	0.1380	0.03327	HIRES
2458628.82058	1.21	4.17	0.1377	0.03307	HIRES
2458632.74785	0.10	4.11	0.1344	0.03318	HIRES
2458632.75135	0.42	4.30	0.1342	0.03320	HIRES
2458632.75491	-1.10	4.16	0.1348	0.03320	HIRES
2458632.85224	-12.75	4.12	0.1339	0.03307	HIRES
2458632.85554	3.56	4.24	0.1337	0.03296	HIRES
2458632.85885	-16.81	4.22	0.1345	0.03304	HIRES
2458633.76878	-1.49	4.40	0.1364	0.03313	HIRES
2458633.77707	2.85	4.53	0.1363	0.03314	HIRES
2458633.78548	-5.73	4.16	0.1364	0.03303	HIRES
2458633.82325	-4.78	4.38	0.1363	0.03301	HIRES
2458633.82716	3.52	4.45	0.1357	0.03300	HIRES
2458633.83163	-7.87	4.53	0.1360	0.03303	HIRES
2458647.75057	-6.88	4.57	0.1350	0.03340	HIRES
2458647.75402	-2.60	4.47	0.1360	0.03335	HIRES
2458647.75759	-4.60	3.77	0.1351	0.03331	HIRES
2458647.82239	6.83	4.60	0.1361	0.03322	HIRES
2458647.82634	0.37	4.18	0.1363	0.03314	HIRES

Table 8 *continued*

Table 8 *(continued)*

Time (BJD_{TDB})	RV (m s^{-1})	RV Unc. (m s^{-1})	S_{HK}	H-alpha	Instrument
2458647.83030	-7.89	4.33	0.1362	0.03339	HIRES
2458650.75680	-9.52	4.33	0.1357	0.03304	HIRES
2458650.76074	-13.46	4.52	0.1359	0.03302	HIRES
2458650.76468	-0.39	4.52	0.1357	0.03304	HIRES
2458650.84263	-12.51	4.40	0.1367	0.03270	HIRES
2458650.84601	-11.60	4.64	0.1362	0.03267	HIRES
2458650.84931	-1.02	4.25	0.1370	0.03270	HIRES
2458651.75457	0.14	4.62	0.1341	0.03348	HIRES
2458651.75841	7.26	4.53	0.1347	0.03341	HIRES
2458651.76254	-11.04	4.43	0.1329	0.03342	HIRES
2458651.81380	-9.22	4.26	0.1361	0.03318	HIRES
2458651.81814	6.26	4.34	0.1359	0.03317	HIRES
2458651.82221	-12.08	4.10	0.1357	0.03317	HIRES
2458659.77465	-15.10	4.48	0.1370	0.03322	HIRES
2458659.77766	-11.07	4.58	0.1368	0.03306	HIRES
2458659.78086	-13.61	4.21	0.1368	0.03306	HIRES
2458660.76770	3.46	4.37	0.1361	0.03314	HIRES
2458660.77131	12.67	4.38	0.1359	0.03303	HIRES
2458660.77482	11.91	4.31	0.1371	0.03314	HIRES
2458665.77561	-5.12	4.17	0.1367	0.03339	HIRES
2458665.77882	-8.38	4.09	0.1370	0.03337	HIRES
2458665.78206	-6.86	4.18	0.1368	0.03345	HIRES
2458679.77419	2.38	4.17	0.1377	0.03294	HIRES
2458679.77729	3.83	4.12	0.1374	0.03288	HIRES
2458679.78036	5.70	4.56	0.1373	0.03288	HIRES
2458709.73744	-8.95	5.03	0.1107	0.03287	HIRES
2458809.13240	-3.77	4.98	0.1236	0.03305	HIRES
2458809.13605	-4.17	4.80	0.1254	0.03298	HIRES
2458809.13960	-20.52	4.87	0.1250	0.03299	HIRES
2458828.12545	9.33	4.22	0.1236	0.03318	HIRES
2458828.12836	-8.55	4.20	0.1238	0.03328	HIRES
2458828.13122	12.10	4.06	0.1250	0.03326	HIRES
2458833.12337	-9.99	4.52	0.1246	0.03333	HIRES
2458833.12694	-4.73	4.81	0.1229	0.03317	HIRES
2458833.13057	-3.89	4.53	0.1250	0.03330	HIRES
2458834.06001	-4.62	4.23	0.1254	0.03302	HIRES
2458834.06378	-11.58	4.15	0.1245	0.03303	HIRES
2458834.06782	-9.07	3.94	0.1255	0.03295	HIRES
2458834.15223	-13.96	3.92	0.1236	0.03314	HIRES
2458834.15545	-17.50	4.11	0.1242	0.03304	HIRES

Table 8 *continued*

Table 8 *(continued)*

Time (BJD_{TDB})	RV (m s^{-1})	RV Unc. (m s^{-1})	S_{HK}	H-alpha	Instrument
2458834.15878	-21.43	4.21	0.1235	0.03304	HIRES
2458878.94352	-3.54	4.98	0.1250	0.03284	HIRES
2458879.94452	-4.14	4.50	0.1242	0.03284	HIRES
2458881.04737	-8.74	4.47	0.1237	0.03324	HIRES
2458881.05080	8.23	4.21	0.1242	0.03307	HIRES
2458881.05422	6.24	4.50	0.1239	0.03313	HIRES
2457759.80567	26.08	6.79	0.1515	–	PFS
2457761.81934	-2.24	7.28	0.1556	–	PFS
2457763.85691	-3.61	6.75	0.1537	–	PFS
2457765.86413	-9.28	7.23	0.1512	–	PFS
2457767.85472	-11.72	6.54	0.1515	–	PFS
2457769.84375	1.40	8.21	0.2536	–	PFS
2458207.69293	8.41	6.81	0.1614	–	PFS
2458265.54169	8.55	5.58	0.1696	–	PFS
2458265.60975	0.00	5.03	0.1669	–	PFS
2458266.54613	0.21	5.40	0.1691	–	PFS
2458266.63963	6.08	5.00	0.1803	–	PFS
2458270.49736	14.74	4.90	0.1594	–	PFS
2458270.65094	8.27	4.74	0.1737	–	PFS
2458271.53219	4.71	4.53	0.1563	–	PFS
2458271.62931	1.16	4.64	0.1614	–	PFS
2458272.49145	6.07	4.65	0.1687	–	PFS
2458272.50365	-15.94	5.76	0.1867	–	PFS
2458272.60086	-3.55	4.61	0.1573	–	PFS
2458292.49251	-3.61	4.53	0.1599	–	PFS
2458292.56916	-7.46	5.09	0.1550	–	PFS
2458294.48588	-2.15	4.84	0.1627	–	PFS
2458294.56182	-17.19	5.39	0.1649	–	PFS
2458296.51344	-12.01	4.90	0.1542	–	PFS
2458299.51510	-6.25	4.93	0.1607	–	PFS
2457781.06111	-5.04	13.21	0.1291	–	APF
2457809.02734	-30.19	22.39	0.1200	–	APF
2457809.05593	-6.34	17.44	0.1431	–	APF
2457815.06470	14.43	12.31	0.1279	–	APF
2457865.81600	-2.68	11.12	0.1335	–	APF
2457809.04177	-38.47	18.68	0.1239	–	APF
2457896.72618	-1.23	14.79	0.1283	–	APF
2457873.86098	0.96	11.55	0.1295	–	APF
2457815.05044	30.82	11.67	0.1247	–	APF
2457901.75498	-3.58	11.65	0.1335	–	APF

Table 8 *continued*

Table 8 *(continued)*

Time (BJD_{TDB})	RV (m s^{-1})	RV Unc. (m s^{-1})	S_{HK}	H-alpha	Instrument
2457882.81860	-44.66	13.42	0.1296	–	APF
2457796.97958	-5.63	17.80	0.1282	–	APF
2457780.91058	48.59	18.83	0.1266	–	APF
2457821.89386	141.13	18.37	0.1297	–	APF
2457822.00237	-5.56	16.55	0.1204	–	APF
2457897.73030	-16.58	12.26	0.1311	–	APF
2457752.06664	11.36	10.45	0.1392	–	APF
2457848.82814	-47.54	24.27	0.1367	–	APF
2457814.83360	-8.39	11.33	0.1328	–	APF
2457896.74040	-18.95	12.14	0.1271	–	APF
2457816.04258	29.95	11.33	0.1302	–	APF
2457780.96595	-5.23	12.58	0.1261	–	APF
2457873.88982	-20.07	13.26	0.1350	–	APF
2457816.05647	-3.25	12.08	0.1615	–	APF
2457781.03551	29.69	15.55	0.1342	–	APF
2457893.73144	-12.69	11.80	0.1297	–	APF
2457893.78716	-21.05	12.27	0.1311	–	APF
2457796.91448	5.30	21.96	0.1281	–	APF
2457873.75443	19.37	12.28	0.1293	–	APF
2457781.10700	-42.78	16.88	0.1438	–	APF
2457882.75310	17.77	12.22	0.1531	–	APF
2457783.84848	-24.83	15.64	0.1158	–	APF
2457893.80928	-158.14	42.60	–	–	APF
2457750.09575	-3.35	11.74	0.1271	–	APF
2457845.84002	-37.50	12.19	0.1267	–	APF
2457901.78421	17.07	11.74	0.1292	–	APF
2457780.91969	12.76	17.97	0.1264	–	APF
2457848.79785	-69.33	24.00	0.2515	–	APF
2457783.87896	-14.96	14.39	0.1374	–	APF
2457814.93242	2.54	10.07	0.1320	–	APF
2457823.76616	87.35	14.36	0.1375	–	APF
2457815.03593	12.47	11.61	0.1320	–	APF
2457847.93237	-61.36	11.48	0.1262	–	APF
2457784.00396	-1.34	11.82	0.1244	–	APF
2457847.94652	-16.56	13.23	0.1318	–	APF
2457901.76933	-16.30	11.76	0.1263	–	APF
2457783.98895	15.76	12.71	0.1350	–	APF
2457752.03791	-2.96	10.43	0.1350	–	APF
2457845.98544	-28.47	13.65	0.1396	–	APF
2457893.79993	-8.99	12.85	0.1385	–	APF

Table 8 *continued*

Table 8 *(continued)*

Time (BJD_{TDB})	RV (m s^{-1})	RV Unc. (m s^{-1})	S_{HK}	H-alpha	Instrument
2457780.90075	0.82	20.01	0.1329	–	APF
2457784.10953	-81.15	15.50	0.1450	–	APF
2457750.06719	52.66	12.77	0.1296	–	APF
2457781.04973	-3.73	14.98	0.1348	–	APF
2457865.80733	-19.26	22.07	0.1329	–	APF
2457847.91817	-20.83	11.73	0.1332	–	APF
2457873.74045	-2.22	11.53	0.1345	–	APF
2457752.05226	25.85	9.94	0.1328	–	APF
2457815.84613	7.36	11.11	0.1281	–	APF
2457823.84886	81.62	14.50	0.1267	–	APF
2457882.74019	-41.25	11.84	0.1340	–	APF
2457814.81938	-6.62	11.75	0.1295	–	APF
2457877.83994	-26.05	12.92	0.1327	–	APF
2457894.74722	2.66	11.74	0.1363	–	APF
2457882.84429	-22.37	13.67	0.1335	–	APF
2457919.74774	9.62	12.86	0.1360	–	APF
2457873.76897	-18.00	13.05	0.1306	–	APF
2457783.86216	0.61	14.70	0.1292	–	APF
2457893.74604	-5.52	11.15	0.1250	–	APF
2457897.71559	-10.66	11.75	0.1322	–	APF
2457823.75089	63.51	15.59	0.1228	–	APF
2457865.83042	1.38	12.02	0.1344	–	APF
2457822.01596	72.13	18.72	0.1306	–	APF
2457796.92414	-77.42	21.74	0.1135	–	APF
2457780.95155	1.04	12.42	0.1285	–	APF
2457877.78376	5.38	11.67	0.1306	–	APF
2457894.71857	-5.35	11.55	0.1319	–	APF
2457815.91674	2.57	11.42	0.1319	–	APF
2457814.84816	-15.17	11.87	0.1258	–	APF
2457877.75768	-52.78	11.60	0.1270	–	APF
2457815.81820	-2.70	11.36	0.1320	–	APF
2457784.01797	3.61	13.70	0.1309	–	APF
2457873.87517	-17.82	13.27	0.1263	–	APF
2457845.85385	-17.22	13.75	0.1340	–	APF
2457822.03064	72.96	18.27	0.1234	–	APF
2457823.73526	158.58	20.04	0.1148	–	APF
2457887.79156	10.47	21.52	0.1353	–	APF
2457823.83544	122.21	14.40	0.1289	–	APF
2457750.08117	8.69	12.42	0.1326	–	APF
2457815.93185	-39.58	11.79	0.1243	–	APF

Table 8 *continued*

Table 8 *(continued)*

Time (BJD_{TDB})	RV (m s^{-1})	RV Unc. (m s^{-1})	S_{HK}	H-alpha	Instrument
2457919.77509	15.30	13.33	0.1288	–	APF
2457877.85293	25.49	12.10	0.1319	–	APF
2457877.77163	-12.37	11.11	0.1318	–	APF
2457815.83197	21.74	11.47	0.1270	–	APF
2457896.71402	-14.85	12.71	0.1296	–	APF
2457893.71726	3.00	10.32	0.1307	–	APF
2457823.82109	50.03	13.31	0.1279	–	APF
2457796.90531	-24.95	21.01	0.1225	–	APF
2457887.81092	-7.28	15.47	0.1321	–	APF
2457816.07010	24.14	13.86	0.1306	–	APF
2457796.98993	-36.61	17.39	0.1185	–	APF
2457829.94568	-14.07	10.74	0.1330	–	APF
2457784.09563	-4.87	12.95	0.1541	–	APF
2457796.96897	30.46	18.35	0.1279	–	APF
2457845.86927	-31.55	13.66	0.1339	–	APF
2457882.76205	9.55	16.04	–	–	APF
2457821.87919	50.01	16.52	0.1379	–	APF
2457814.91859	-13.03	9.80	0.1325	–	APF
2457894.80200	16.97	11.99	0.1304	–	APF
2457894.81491	15.35	12.04	0.1308	–	APF
2457894.73280	-12.60	10.89	0.1350	–	APF
2457829.96052	-11.24	11.38	0.1287	–	APF
2457829.97503	-2.62	11.61	0.1351	–	APF
2457897.74280	6.85	12.72	0.1250	–	APF
2457780.98023	13.16	12.70	0.1332	–	APF
2457919.76193	3.86	12.00	0.1334	–	APF
2457815.90276	15.11	10.73	0.1280	–	APF
2457887.80079	-10.67	20.01	0.1378	–	APF
2457845.95683	-27.37	12.47	0.1294	–	APF
2457882.83131	-38.41	14.90	0.1309	–	APF
2457821.86260	44.47	15.33	0.1332	–	APF
2457848.81036	-130.55	25.27	0.1204	–	APF
2457814.94576	1.03	9.37	0.1291	–	APF
2457845.97122	-38.39	12.72	0.1342	–	APF
2457894.78750	8.53	10.56	0.1274	–	APF

S_{HK} values have an uncertainty of 0.001 for HIRES data, 0.002 for APF data, and no calculated uncertainties for PFS data.

Table 9. GJ 9827 Photometry

Time (HJD)	Differential Magnitude (Cousins R)
2458384.8398	-3.29860
2458387.7886	-3.29043
2458388.7836	-3.29695
2458389.7598	-3.29301
2458390.7934	-3.29492
2458395.8109	-3.29757
2458396.7518	-3.29810
2458397.7672	-3.29389
2458401.7730	-3.29437
2458409.7743	-3.29824
2458411.7562	-3.29593
2458416.7611	-3.29737
2458417.7244	-3.29568
2458418.7359	-3.29437
2458419.7340	-3.29448
2458420.7310	-3.29879
2458424.7217	-3.30008
2458425.7338	-3.28865
2458426.7161	-3.29505
2458428.7217	-3.29477
2458429.7013	-3.29479
2458430.7246	-3.29014
2458431.7200	-3.29774
2458432.7074	-3.29444
2458433.6980	-3.29743
2458434.6915	-3.29221
2458435.7153	-3.29915
2458438.6970	-3.30280
2458439.7007	-3.29541
2458442.7045	-3.30265
2458443.7110	-3.29193
2458447.7030	-3.28811
2458448.6802	-3.29624
2458456.6973	-3.29770
2458462.6936	-3.29643
2458465.6939	-3.29154
2458466.6406	-3.29506
2458472.6551	-3.29889
2458473.6821	-3.29741
2458477.6708	-3.29311
2458487.6505	-3.30077

Table 9 *continued*

Table 9 *(continued)*

Time (HJD)	Differential Magnitude (Cousins R)
2458488.6392	-3.29675
2458510.5919	-3.29905
2458630.9510	-3.29773
2458635.9774	-3.29121
2458639.9574	-3.28977
2458640.9686	-3.29189
2458641.9467	-3.28610
2458654.9693	-3.30466
2458655.9418	-3.29611
2458657.9366	-3.29868
2458757.7474	-3.29591
2458762.7384	-3.29828
2458763.8894	-3.29123
2458765.7077	-3.30108
2458766.7137	-3.29908
2458770.7195	-3.29695
2458771.6987	-3.29525
2458775.7327	-3.29347
2458777.7144	-3.29992
2458778.6961	-3.29596
2458780.6850	-3.29421
2458781.7094	-3.28570
2458784.6903	-3.29402
2458787.6802	-3.29677
2458788.7024	-3.29800
2458800.7053	-3.29736
2458801.6652	-3.30072
2458802.6866	-3.29158
2458831.7012	-3.30000
2458833.6352	-3.29162
2458860.6088	-3.29597
2458867.5926	-3.29273
2458876.5765	-3.29225

Table 10. HD 106315 Photometry

Time (HJD)	Differential Magnitude ((b+y)/2)
2458159.9462	1.58370
2458161.9455	1.58287
2458162.8071	1.58217

Table 10 *continued*

Table 10 *(continued)*

Time (HJD)	Differential Magnitude ((b+y)/2)
2458172.7803	1.58193
2458174.7746	1.58083
2458174.9086	1.58407
2458176.8481	1.58453
2458183.8548	1.58830
2458184.7545	1.58647
2458184.8741	1.58447
2458189.7523	1.58600
2458195.7926	1.58200
2458195.8678	1.58800
2458197.7836	1.58283
2458197.8585	1.58413
2458204.7111	1.58447
2458204.8259	1.58257
2458205.7376	1.58827
2458205.7839	1.58210
2458210.7527	1.58693
2458210.8097	1.58093
2458211.7425	1.58367
2458212.7486	1.58580
2458212.8103	1.58507
2458213.7943	1.58350
2458216.7387	1.58667
2458218.7464	1.58583
2458220.8272	1.59000
2458223.7525	1.58690
2458228.7301	1.58970
2458229.7351	1.58503
2458231.6962	1.58663
2458241.7346	1.58417
2458242.7333	1.58747
2458250.7291	1.58127
2458256.7137	1.58497
2458257.7085	1.58543
2458258.6988	1.58087
2458266.6928	1.59070
2458267.7002	1.58433
2458272.6969	1.58287
2458273.6955	1.58683
2458277.6920	1.58887

ACKNOWLEDGMENTS

We thank the anonymous reviewer for their time and helpful comments.

M.R.K is supported by the NSF Graduate Research Fellowship, grant No. DGE 1339067.

C.P. is supported by the Technologies for Exo-Planetary Science (TEPS) CREATE program and further acknowledges financial support by the Fonds de Recherche Québécois—Nature et Technologie (FRQNT; Québec).

G.W.H. acknowledges long-term support from NASA, NSF, Tennessee State University, and the State of Tennessee through its Centers of Excellence program.

L.M.W. is supported by the Beatrice Watson Parrent Fellowship and NASA ADAP Grant 80NSSC19K0597.

P.D. acknowledges support from a National Science Foundation Astronomy and Astrophysics Postdoctoral Fellowship under award AST-1903811.

JMAM gratefully acknowledges support from the National Science Foundation Graduate Research Fellowship Program under Grant No. DGE-1842400. JMAM also thanks the LSSTC Data Science Fellowship Program, which is funded by LSSTC, NSF Cybertraining Grant No. 1829740, the Brinson Foundation, and the Moore Foundation; his participation in the program has benefited this work.

The authors wish to recognize and acknowledge the very significant cultural role and reverence that the summit of Maunakea has always had within the indigenous Hawaiian community. We are most fortunate to have the opportunity to conduct observations from this mountain.

Some of the observations in the paper made use of the High-Resolution Imaging instrument Zorro. Zorro was funded by the NASA Exoplanet Exploration Program and built at the NASA Ames Research Center by Steve B. Howell, Nic Scott, Elliott P. Horch, and Emmett Quigley. Zorro is mounted on the Gemini South telescope of the international Gemini Observatory, a program of NSF's OIR Lab, which is managed by the Association of Universities for Research in Astronomy (AURA) under a cooperative agreement with the National Science Foundation.

This work is based in part on observations made with the *Spitzer* Space Telescope, which was operated by the Jet Propulsion Laboratory, California Institute of Technology under a contract with NASA. Support for this work was provided by NASA through an award issued by JPL/Caltech.

This research has made use of the Exoplanet Follow-up Observing Program (ExoFOP), which is operated by the California Institute of Technology, under contract with the National Aeronautics and Space Administration.

Part of the research was carried out at the Jet Propulsion Laboratory, California Institute of Technology, under a contract with the National Aeronautics and Space Administration (80NM0018D0004).

This work has made use of data from the European Space Agency (ESA) mission *Gaia* (https://www.cosmos.esa.int/gaia), processed by the *Gaia* Data Processing and Analysis Consortium (DPAC, https://www.cosmos.esa.int/web/gaia/dpac/consortium). Funding for the DPAC has been provided by national institutions, in particular the institutions participating in the *Gaia* Multilateral Agreement.

Facilities: Keck:I(HIRES), Magellan:Clay(PFS), Spitzer, APF, TSU:AIT, Gemini:South(Zorro)

Software: `radvel` (Fulton et al. 2018), `batman` (Kreidberg 2015), `SpecMatch-Emp` (Yee et al. 2017), `isoclassify` (Huber et al. 2017), `spock` (Tamayo et al. 2020), `rebound` (Rein & Liu 2011), `numpy` (van der Walt et al. 2011), `astropy` (Astropy Collaboration et al. 2013), `emcee` (Foreman-Mackey et al. 2013)

REFERENCES

Albrecht, S., Winn, J. N., Marcy, G. W., et al. 2013, ApJ, 771, 11, doi: 10.1088/0004-637X/771/1/11

Astropy Collaboration, Robitaille, T. P., Tollerud, E. J., et al. 2013, A&A, 558, A33, doi: 10.1051/0004-6361/201322068

Barros, S. C. C., Gosselin, H., Lillo-Box, J., et al. 2017, A&A, 608, A25, doi: 10.1051/0004-6361/201731276

Batalha, N. E., Lewis, T., Fortney, J. J., et al. 2019, arXiv e-prints. https://arxiv.org/abs/1910.00076

Berardo, D., Crossfield, I. J. M., Werner, M., et al. 2019, AJ, 157, 185, doi: 10.3847/1538-3881/ab100c

Butler, R. P., Marcy, G. W., Williams, E., et al. 1996, PASP, 108, 500, doi: 10.1086/133755

Chaplin, W. J., Cegla, H. M., Watson, C. A., Davies, G. R., & Ball, W. H. 2019, AJ, 157, 163, doi: 10.3847/1538-3881/ab0c01

Claret, A., & Bloemen, S. 2011, A&A, 529, A75, doi: 10.1051/0004-6361/201116451

Crane, J. D., Shectman, S. A., & Butler, R. P. 2006, in Society of Photo-Optical Instrumentation Engineers (SPIE) Conference Series, Vol. 6269, Society of Photo-Optical Instrumentation Engineers (SPIE) Conference Series, 626931, doi: 10.1117/12.672339

Crane, J. D., Shectman, S. A., Butler, R. P., et al. 2010, in Society of Photo-Optical Instrumentation Engineers (SPIE) Conference Series, Vol. 7735, Ground-based and Airborne Instrumentation for Astronomy III, 773553, doi: 10.1117/12.857792

Crane, J. D., Shectman, S. A., Butler, R. P., Thompson, I. B., & Burley, G. S. 2008, in Society of Photo-Optical Instrumentation Engineers (SPIE) Conference Series, Vol. 7014, Ground-based and Airborne Instrumentation for Astronomy II, 701479, doi: 10.1117/12.789637

Crossfield, I. J. M., Ciardi, D. R., Isaacson, H., et al. 2017, AJ, 153, 255, doi: 10.3847/1538-3881/aa6e01

Deming, D., Knutson, H., Kammer, J., et al. 2015, ApJ, 805, 132, doi: 10.1088/0004-637X/805/2/132

Eaton, J. A., Henry, G. W., & Fekel, F. C. 2003, in Astrophysics and Space Science Library, Vol. 288, Astrophysics and Space Science Library, ed. T. D. Oswalt, 189, doi: 10.1007/978-94-010-0253-0_38

Fazio, G. G., Hora, J. L., Allen, L. E., et al. 2004, ApJS, 154, 10, doi: 10.1086/422843

Figueira, P., Pont, F., Mordasini, C., et al. 2009, A&A, 493, 671, doi: 10.1051/0004-6361:20078951

Foreman-Mackey, D., Hogg, D. W., Lang, D., & Goodman, J. 2013, PASP, 125, 306, doi: 10.1086/670067

Frandsen, S., & Lindberg, B. 1999, in Astrophysics with the NOT, ed. H. Karttunen & V. Piirola, 71

Fulton, B. J., Petigura, E. A., Blunt, S., & Sinukoff, E. 2018, PASP, 130, 044504, doi: 10.1088/1538-3873/aaaaa8

Fulton, B. J., Weiss, L. M., Sinukoff, E., et al. 2015, ApJ, 805, 175, doi: 10.1088/0004-637X/805/2/175

Fulton, B. J., Petigura, E. A., Howard, A. W., et al. 2017, AJ, 154, 109, doi: 10.3847/1538-3881/aa80eb

Gaia Collaboration, Prusti, T., de Bruijne, J. H. J., et al. 2016, A&A, 595, A1, doi: 10.1051/0004-6361/201629272

Gaia Collaboration, Brown, A. G. A., Vallenari, A., et al. 2018, A&A, 616, A1, doi: 10.1051/0004-6361/201833051

Haywood, R. D., Collier Cameron, A., Queloz, D., et al. 2014, MNRAS, 443, 2517, doi: 10.1093/mnras/stu1320

Henry, G. W. 1999, PASP, 111, 845, doi: 10.1086/316388

Howard, A. W., Johnson, J. A., Marcy, G. W., et al. 2010, ApJ, 721, 1467, doi: 10.1088/0004-637X/721/2/1467

Howell, S. B., Everett, M. E., Sherry, W., Horch, E., & Ciardi, D. R. 2011, AJ, 142, 19, doi: 10.1088/0004-6256/142/1/19

Huber, D., Zinn, J., Bojsen-Hansen, M., et al. 2017, ApJ, 844, 102, doi: 10.3847/1538-4357/aa75ca

Isaacson, H., & Fischer, D. 2010, ApJ, 725, 875, doi: 10.1088/0004-637X/725/1/875

Kasper, D., Bean, J. L., Oklopčić, A., et al. 2020, arXiv e-prints, arXiv:2007.12968. https://arxiv.org/abs/2007.12968

Kempton, E. M. R., Bean, J. L., Louie, D. R., et al. 2018, PASP, 130, 114401, doi: 10.1088/1538-3873/aadf6f

Kosiarek, M. R., & Crossfield, I. J. M. 2020, AJ, 159, 271, doi: 10.3847/1538-3881/ab8d3a

Kraft, R. P. 1967, ApJ, 150, 551, doi: 10.1086/149359

Kreidberg, L. 2015, PASP, 127, 1161, doi: 10.1086/683602

Kreidberg, L., Mollière, P., Crossfield, I. J. M., et al. 2020, arXiv e-prints, arXiv:2006.07444. https://arxiv.org/abs/2006.07444

Lendl, M., Ehrenreich, D., Turner, O. D., et al. 2017, A&A, 603, L5, doi: 10.1051/0004-6361/201731278

Lopez, E. D., & Fortney, J. J. 2014, ApJ, 792, 1, doi: 10.1088/0004-637X/792/1/1

Luri, X., Brown, A. G. A., Sarro, L. M., et al. 2018, A&A, 616, A9, doi: 10.1051/0004-6361/201832964

Mayor, M., Pepe, F., Queloz, D., et al. 2003, The Messenger, 114, 20

Nava, C., López-Morales, M., Haywood, R. D., & Giles, H. A. C. 2019, arXiv e-prints, arXiv:1911.04106. https://arxiv.org/abs/1911.04106

Niraula, P., Redfield, S., Dai, F., et al. 2017, AJ, 154, 266, doi: 10.3847/1538-3881/aa957c

Owen, J. E., & Campos Estrada, B. 2019, Monthly Notices of the Royal Astronomical Society, 491, 5287, doi: 10.1093/mnras/stz3435

Owen, J. E., & Wu, Y. 2013, ApJ, 775, 105, doi: 10.1088/0004-637X/775/2/105

—. 2017, ApJ, 847, 29, doi: 10.3847/1538-4357/aa890a

Petigura, E. A., Schlieder, J. E., Crossfield, I. J. M., et al. 2015, ApJ, 811, 102, doi: 10.1088/0004-637X/811/2/102

Petigura, E. A., Howard, A. W., Marcy, G. W., et al. 2017, AJ, 154, 107, doi: 10.3847/1538-3881/aa80de

Prieto-Arranz, J., Palle, E., Gandolfi, D., et al. 2018, A&A, 618, A116, doi: 10.1051/0004-6361/201832872

Radovan, M. V., Lanclos, K., Holden, B. P., et al. 2014, in Society of Photo-Optical Instrumentation Engineers (SPIE) Conference Series, Vol. 9145, Proc. SPIE, 91452B, doi: 10.1117/12.2057310

Rein, H., & Liu, S.-F. 2011, REBOUND: Multi-purpose N-body code for collisional dynamics. http://ascl.net/1110.016

Rice, K., Malavolta, L., Mayo, A., et al. 2019, MNRAS, 484, 3731, doi: 10.1093/mnras/stz130

Robertson, P., Endl, M., Cochran, W. D., & Dodson-Robinson, S. E. 2013, ApJ, 764, 3, doi: 10.1088/0004-637X/764/1/3

Rodriguez, J. E., Vanderburg, A., Eastman, J. D., et al. 2018, AJ, 155, 72, doi: 10.3847/1538-3881/aaa292

Rodriguez, J. E., Zhou, G., Vanderburg, A., et al. 2017, AJ, 153, 256, doi: 10.3847/1538-3881/aa6dfb

Rogers, L. A., & Seager, S. 2010, ApJ, 712, 974, doi: 10.1088/0004-637X/712/2/974

Tamayo, D., Cranmer, M., Hadden, S., et al. 2020, arXiv e-prints, arXiv:2007.06521. https://arxiv.org/abs/2007.06521

Telting, J. H., Avila, G., Buchhave, L., et al. 2014, Astronomische Nachrichten, 335, 41, doi: 10.1002/asna.201312007

Teske, J. K., Wang, S., Wolfgang, A., et al. 2018, AJ, 155, 148, doi: 10.3847/1538-3881/aaab56

van der Walt, S., Colbert, S. C., & Varoquaux, G. 2011, Computing in Science and Engineering, 13, 22, doi: 10.1109/MCSE.2011.37

Vogt, S. S., Allen, S. L., Bigelow, B. C., et al. 1994, in Proc. SPIE, Vol. 2198, Instrumentation in Astronomy VIII, ed. D. L. Crawford & E. R. Craine, 362, doi: 10.1117/12.176725

Vogt, S. S., Radovan, M., Kibrick, R., et al. 2014, PASP, 126, 359, doi: 10.1086/676120

Weiss, L. M., Rogers, L. A., Isaacson, H. T., et al. 2016, ApJ, 819, 83, doi: 10.3847/0004-637X/819/1/83

Winn, J. N. 2010, Exoplanet Transits and Occultations, ed. S. Seager, 55–77

Yee, S. W., Petigura, E. A., & von Braun, K. 2017, ApJ, 836, 77, doi: 10.3847/1538-4357/836/1/77

Zeng, L., & Sasselov, D. 2013, PASP, 125, 227, doi: 10.1086/669163

Zeng, L., Sasselov, D. D., & Jacobsen, S. B. 2016, ApJ, 819, 127, doi: 10.3847/0004-637X/819/2/127

Zhou, G., Rodriguez, J. E., Vanderburg, A., et al. 2018, AJ, 156, 93, doi: 10.3847/1538-3881/aad085